REVIEW

Check for updates

Molecular dynamics simulations of phase change materials for thermal energy storage: a review

Hossein Tafrishi,[a] Sadegh Sadeghzadeh [iD] *[b] and Rouhollah Ahmadi [iD] [c]

Phase change materials (PCM) have had a significant role as thermal energy transfer fluids and nanofluids and as media for thermal energy storage. Molecular dynamics (MD) simulations, can play a significant role in addressing several thermo-physical problems of PCMs at the atomic scale by providing profound insights and new information. In this paper, the reviewed research is classified into five groups: pure PCM, mixed PCM, PCM containing nanofillers, nano encapsulated PCM, and PCM in nanoporous media. A summary of the equilibrium and non-equilibrium MD simulations of PCMs and their results is presented as well. The primary results of the simulated systems are demonstrated to be efficient in manufacturing phase change materials with better thermal energy storage features. The goals of these studies are to achieve higher thermal conductivity, higher thermal capacity, and lower density change, determine the melting point, and understand the molecular behaviors of PCM composites. A molecular dynamics-based grouping (PCM simulation table) was presented that is very useful for the future roadmap of PCM simulation. In the end, the PCFF force field is presented in detail and a case problem is studied for more clarity. The results show that simulating the PCMs with a similar strategy could be performed systematically. Results of investigations of thermal conductivity enhancement showed that this characteristic can be increased at the nano-scale by the orientation of PCM molecules.

1 Introduction

One of the most significant problems at the moment is meeting rising energy needs. The estimated global energy demand is about 15 TW per annum.[1] In several types of buildings that have major heating needs, heat storage may be used.[2] Thermal energy storage is achieved through a variety of techniques: sensible heat storage method, latent heat storage method, and thermochemical heat storage method, or a mixture of these methods.[3,4] In the reverse cycle, thermal energy storage (TES) may be obtained by cooling, melting, heating, freezing, or evaporating a substance in which case energy is obtained as heat.[5,6] Latent heat storage using PCMs provides a high energy storage capacity and enables the storage of thermal energy at a constant temperature corresponding to the storage material's phase transition temperature.[7,8] For PCMs, phase transition can be solid–liquid, liquid–gas, or solid–solid. Polymorphic transfer from one crystalline state to another can be observed in the solid–solid thermal energy storage or PCMs that are shape stabilized. Solids–solids a good feature they have is that they

change very little in volume and have good design flexibility, but usually have less latent heat than solid–liquid and liquid–gas. The use of solid–solid PCMs can prevent problems such as permeation at temperatures above the phase changing temperature. This is a very important and good property of the large leakage problem in solid–liquid PCMs. The general grading of PCMs is shown in Fig. 1.

Methods have been considered in the last years for enhancing the physical and thermal features of PCMs. Combining PCMs with nanomaterials will lead to better properties of thermal storage than the bulk PCMs (*i.e.*, their pure state). That can result in the following benefits:[9]

● Increased thermal conductivity of PCMs.

● Enhance thermal consistency of PCMs.

● Better performance and increased storage of heat in some cases.

The heat transfer properties of magnesium nitrate hexahydrate PCM ($Mg(NO_3)_2 \cdot 6H_2O$) include nano graphite (NG) and multiwalled carbon nanotube (MWCNT) composites were investigated by Kardam *et al.*[10] Their work found that nano-PCM melting and freezing levels increased by 48% and 77% respectively. Nevertheless, these percentages were 24 percent and 15 percent respectively for PCM composites containing nano graphite (0.6 percent by weight). Graphene nanoplatelets (GNPs) were supplemented to improve Eicosan's thermal conductivity.[11] The thermal conductivity of PCM increased by 400 percent in the largest volume of graphene, 10 percent by

[a] *MSc Student of Energy Systems Engineering, School of Advanced Technologies, Iran University of Science and technology, Tehran, Iran*

[b] *Associate Professor of Nanotechnology Engineering, School of Advanced Technologies, Iran University of Science and Technology, Tehran, Iran. E-mail: sadeghzadeh@iust.ac.ir*

[c] *Associate Professor of Energy Systems Engineering, School of Advanced Technologies, Iran University of Science and Technology, Tehran, Iran*
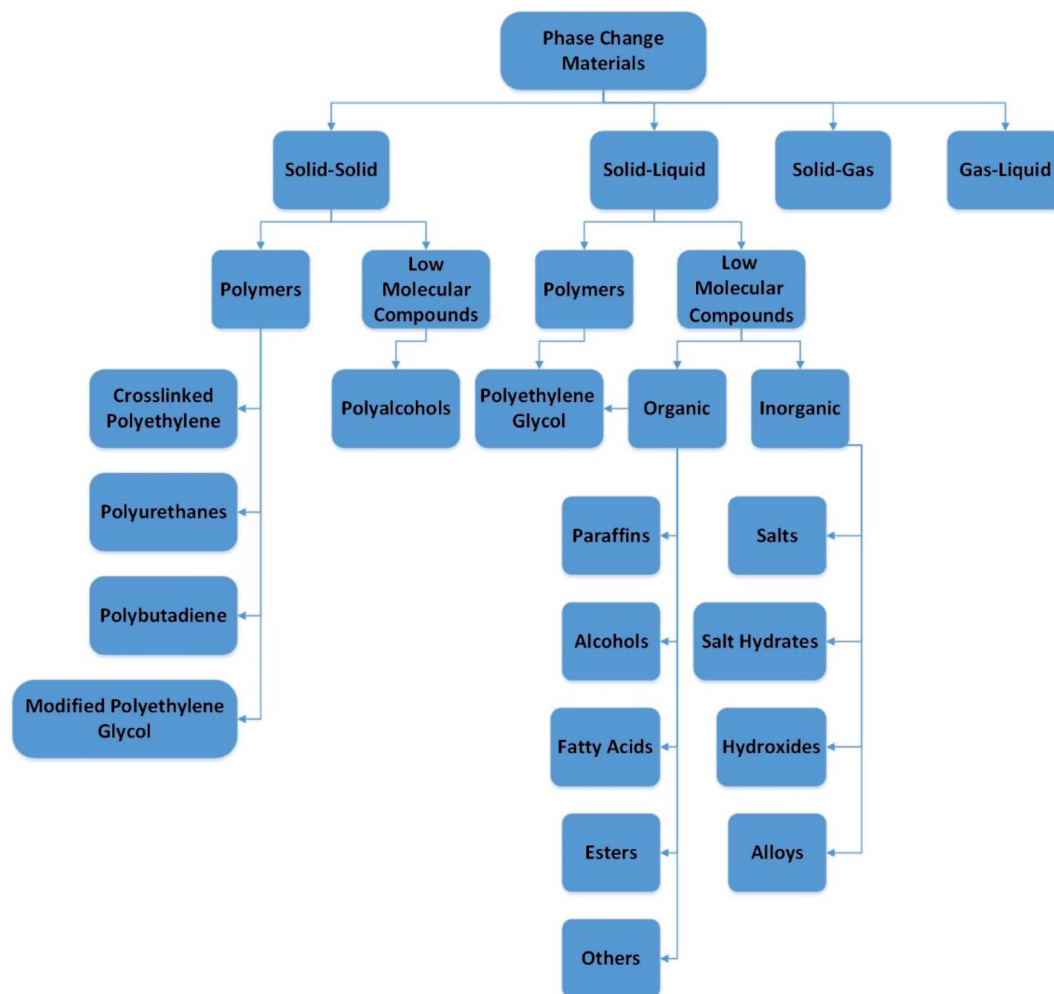
Fig. 1   Phase change materials division (this figure has been adapted from ref. 5 with permission from Elsevier, copyright 2014).

weight of graphene at 10 °C. Harish *et al.*[12] have focused on the design and manufacture of lauric acid PCM nano-composites including graphene sheets (nanoplatelets). The result was that the presence of graphene nanoplatelets by 1% volume enhanced the thermal conductivity by about 230%. The findings of the DSC showed that the phase shift and melting temperature enthalpy remained the same as for the pure material. Nitrogen-doped graphene as a nano-additive was used by Mehrali *et al.* for palmitic acid.[13] The consequence of this analysis was that the thermal conductivity was enhanced by about 500% at 35 °C (for the maximum amount of doped graphene 5% by weight). In another investigation, Ji *et al.* demonstrated that the use of ultrathin-graphite foams (0.8 to 1.2% by volume) in a PCM can enhance the thermal conductivity of the PCM by about 18 times.[14] Nevertheless, this did not have a major impact on the temperature of the PCM melting point. Qi *et al.*[15] developed a composite made of polyethylene glycol, graphene oxide, and graphene nanoplatelets containing 2 wt% graphene oxide and 4 wt% graphene nanoplatelets. The thermal conductivity of this mixture was 1.72 W mK^{-1}, which is 490% more than the thermal conductivity of pure polyethylene

glycol. Wu *et al.* worked on the melting and glaciating properties of paraffin-containing copper nanoparticles.[16] Empirical outcomes showed that the addition of 2 wt% copper nanoparticles to paraffin increased thermal conductivity by 14.2% for the solid state and 18.1% for the liquid state. The organic ester PCM analyzed by Parameshwaran *et al.* comprises a mixture of silver–titania with a mass percentage of 0.1 to 1.5.[17] This hybrid nano-PCM exhibited higher thermal conductivity, rising from 0.286 to 0.538 W mK^{-1}.[18]

Computer use to investigate material properties dates back to the 1950s. Metropolis *et al.*,[19] and Alder and Wainwright[20] respectively performed the first simulations of the Monte Carlo (MC) and molecular dynamics (MD) fluid models. Since that time, continuous advances in hardware and software have led to rapid growth in this area and current MD simulations. Molecular dynamics simulation can be a useful method for investigating the inter-molecular behavior of PCMs or designing new PCMs with better characteristics. This method can be used for simulating nano-enhanced PCMs (NEPCM) that contain nano-structures or are nano-encapsulated. However pure PCM materials with no nano-enhancing also can be investigated and

help to understand the material's behavior at the nano-scale. This paper studies the molecular dynamics simulations of phase change materials, the research had done before and the future needs of this kind of study. Some research works used other methods such as the density functional theory (DFT) to study phase change materials and related structures. For example, M. Micciarelli *et al.* have presented a detailed study of the excited state properties of 5-benzyluracil (5BU) in the gas phase and in implicit solvent using different electronic structure approaches ranging from time-dependent density functional theory in the linear response regime (LR-TDDFT) to a set of different wave-function-based methods for excited states, namely perturbed coupled cluster (CC2), algebraic diagrammatic construction method to second-order (ADC(2)), and perturbed configuration interaction (CIS(D)).[21] Valadan *et al.*[22] have combined fluorescence up-conversion and time-correlated single-photon counting experiments to investigate the 5-benzyl uracil excited state dynamics in methanol from 100 fs up to several ns. Micciarelli *et al.* have investigated the photophysical and photochemical properties of 5-benzyluracil and 5,6-benzyluracil, both experimentally and theoretically.[23] However, here the molecular dynamics approach is focused, and DFT works were not included.

2 Molecular dynamics approach

A simulation on a molecular scale consists of three main steps: first, model building, second, calculating the molecular path, and third, analyzing the atoms' paths and calculating the thermodynamic properties. The second stage forms the basis for the simulation, and at this stage, the method of measuring the molecular positions is to differentiate various methods of simulation. In molecular dynamics, situations are derived from the resolvent of differential motion equations and are thus associated temporally. This method neglects electronic reactions. Although this method in many cases simulates system behavior with high accuracy, it is not able to calculate properties that are dependent on the electronic interaction. Quantum mechanics methods explicitly take into account the electronic structure of atoms and, if applied at any stage of the simulation, to obtain energy, very good results are obtained. This approach is used to solve problems that cannot be solved by classical methods of molecular dynamics, such as chemical reactions where chemical bonds are broken or formed, but these quantum methods are computationally time-consuming and are typically used for systems with a maximum of several tens of atoms. The Schrödinger equation is replaced, in classical molecular mechanics, by the Newton equation. Assuming that the thermal de Broglie wavelength is smaller than the smallest atomic distance is assuming this condition. This situation is especially valid for atoms that are heavier than hydrogen, at high temperatures. So a molecular dynamics simulation is an explicit technique for generating a dynamic trajectory for an N particles system using Newton's motion equations.[24] We need a set of initial conditions (the positions and velocities of each atom), a good model (force field) to demonstrate the forces of the interparticles' interactions, and the boundary conditions to

be used. Then we need to solve the classic equation of movement:

$$m_i \frac{\mathrm{d}^2 r_i}{\mathrm{d}t^2} = f_i = -\frac{\partial}{\partial r_i} U(r_1, \ r_2, \ r_3, \ \ldots, \ r_n) \qquad (1)$$

where $U(r_1, r_2, r_3, \ldots, r_n)$ is the potential energy depends on the coordinates of the n particles that are called force field. In the above equation, r_i is the position vector of the ith atom, f_i is the force applied to each particle, and m_i is the ith atom's mass, and t is the time. Weak bulk forces, such as gravity, typically have very little effect on the nanoparticles' energy changes, so they are (or can be) ignored in molecular dynamics.

The molecular dynamics method can help to design, devise, and invent newer and better thermal energy storage materials like NEPCMs (nano-enhanced phase change materials) or NFPCMs (nano-fluid phase change materials). This method also helps to solve the prevailing problems (like low thermal conductivity and capacity) or better understand the unknown molecular behavior of energy storage materials.

3 Background overview

The works on the molecular dynamics simulation of phase change materials will be discussed in this section. Table 1 summarizes those studies. These researches are categorized into 5 groups (as shown in Fig. 2): nano-enhanced phase change materials with nanofillers (one type nanofiller or hybrid nanofillers), pure phase change materials, mixtures of different PCMs, nano-encapsulated PCM (or PCM in micro/nanocapsules), and porous media for PCMs (micro/nanoporous materials containing PCM). The research performed in all those studies will be briefly clarified in the following. It should be noted that the first 19 papers in Table 1 deal with MD simulations of pure PCMs, 20 to 24 PCM mixtures, 25 to 51 the use of nanoparticles in phase change materials, 52 to 57 refer to simulated micro/nano-encapsulated PCMs with MD, and the last two articles (numbers 58 and 59) are related to porous media incorporating a PCM.

In molecular dynamics, the size of the simulation box is limited and can affect the measured heat transfer attributes.[25,26] However, because running MD simulations are time-consuming even with high-speed clusters, a good and enough box size choice should be acceptable for accepting and publishing the MD studies. Because the needed investigations are much more than those have been done so far and the size dependency of PCM materials was not very obvious in the literature. In other words, usually with increasing the simulation box dimensions and number of atoms, the results will not very change after an optimized value of box length and atom numbers.

3.1 Pure PCM simulations

Pure PCM materials MD simulations will discuss in this section. Zerbi *et al.*[28] investigated *n*-nonadecane ($C_{19}H_{40}$) experimentally and numerically using the Snyder force field.[27] They investigated some structural properties such as *trans* and *gauche* conformations of nonadecane. Esselink *et al.*[31] studied the

Table 1 Molecular dynamics simulation studies of phase change materials (PCMs)

No.	Authors	Date	Simulated materials	Simulation software	Force fields	The main result
1	Zerbi et al.[28]	1981	n-Nonadecane ($C_{19}H_{40}$)	Not mentioned	Snyder force field[27]	A model for the mechanism of phase transition is proposed
2	Esselink et al.[31]	1994	n-Alkanes (butane to dodecane)	Not mentioned	Ryckaert and Bellemans Potential,[29] LJ[a][30]	A new method to identify crystalline regions and compute the crystallization rate
3	Shimizu and Yamamoto[32]	2000	n-Decane ($C_{10}H_{22}$)	Not mentioned	Various potentials	The film is more stable when the surface chains are lying perpendicular to the surface
4	Tsuchiya et al.[37]	2001	C_8H_{18}, $C_{10}H_{22}$, $C_{12}H_{26}$, $C_{14}H_{30}$, $C_{16}H_{34}$	Not mentioned	PCFF,[b][33–36] LJ	The melting point of normal alkanes, using the NPT ensemble
5	Zhen Li and Yamamoto[40]	2001	n-Nonadecane ($C_{19}H_{40}$)	Not mentioned	A special force field from ref. 38, LJ from ref. 39	Surface freezing was described in n-alkanes
6	Mavrantza et al.[41]	2001	Polyethylene (some different chain alkanes)	CERIUS-2	COMPASS[c][33]	The wave number shift of the CH_2 stretching bands is related to temperature with a slope of -0.033 cm$-^1$ K^{-1}
7	Waheed et al.[43]	2001	n-Eicosane ($C_{20}H_{42}$)	Not mentioned	PYS[d] force field,[42] LJ	The temperature dependence of crystallization is analyzed in terms of Ziabicki's rate model
8	Marbeuf and Brown[45]	2006	n-Alkanes $C_{18}H_{38}$, $C_{19}H_{40}$, and $C_{20}H_{42}$	DL-POLY[44]	COMPASS	Transient analogs of the RI and RII phases of the odd alkanes are found on melting C18H38 and C20H42
9	Diama et al.[47]	2009	Tetracosane (n-$C_{24}H_{50}$), dotriacontane (n-$C_{32}H_{66}$)	Not mentioned	Weber,[46] LJ	The introduction of gauche defects into the alkane chains drives a melting transition to a monolayer fluid phase
10	Jayaraman et al.[49]	2009	Molten salts ($LiNO_3$, $NaNO_3$, KNO_3)	LAMMPS[e][48]	Buckingham	Very small free-energy differences between the crystal and liquid phases can result in large differences in computed melting point
11	Yi and Rutledge[50]	2011	n-Eicosane ($C_{20}H_{42}$)	LAMMPS	PYS	Fitting the free energy curve to the cylindrical nucleus model, the solid–liquid interfacial free energies are calculated
12	Rao et al.[51]	2012	Paraffin (nonadecane)	Materials Studio	COMPASS	The simulated phase transition temperature of n-nonadecane under high pressure is higher than that under atmospheric pressure
13	Rastgarkafshgarkolaei et al.[53]	2016	Paraffin ($C_{20}H_{42}$, $C_{24}H_{50}$, $C_{26}H_{54}$, and $C_{30}H_{62}$)	LAMMPS	NERD,[52] LJ	A very slight rise in thermal conductivity values as the number of carbon atoms of the chain increases
14	Ni et al.[54]	2019	Molten salts ($LiNO_3$, $NaNO_3$, KNO_3)	LAMMPS	Buckingham	All details work well in predicting the properties of both single nitrate salts and their mixtures
15	Cui et al.[55]	2019	Molten salts (NaCl, KCl, and their mixture)	LAMMPS	EIM	Binary NaCl/KCl systems have also been investigated
16	B. Feng et al.[57]	2019	Solid–solid polyol PCM (pentaerythritol)	LAMMPS	GROMOS[56]	The thermal conductivity of PE is reduced by half after the α-to-γ phase change
17	Y. Feng et al.[59]	2019	Fatty acid (octadecanoic acid)	LAMMPS	CHARMM[58]	The nanochain forms exhibit more phonon scattering by high-level phonon mismatch

Table 1 (Contd.)

No.	Authors	Date	Simulated materials	Simulation software	Force fields	The main result
18	B. Feng et al.[60]	2020	Monohydric alcohols ($C_{12}H_{26}O$, $C_{14}H_{30}O$, and $C_{16}H_{34}O$)	LAMMPS	GROMOS, LJ	The stronger interfacial energy was found to lead to better thermal conductivity
19	B. Feng et al.[61]	2020	Monohydric alcohols: 1-dodecanol ($C_{12}H_{26}O$), 1-tetradecanol ($C_{14}H_{30}O$), 1-hexadecanol ($C_{16}H_{34}O$)	LAMMPS	GROMOS, LJ	The high interfacial heat transfer rate is related to the stronger intermolecular interactions
20	Wentzel and Milner[64]	2010	C_{23} and mixed C_{21}–C_{23} normal alkanes	GROMACS	OPLSAA,[62] flexible Williams[63]	Slower temperature scans may be necessary to properly investigate weakly first-order transitions
21	Rao et al.[65]	2012	Paraffin (nonadecane) and water slurry	Materials Studio	COMPASS	Mixing the n-nonadecane into water decreased mobility but increased the energy storage capacity
22	Rao et al.[66]	2013	Nonadecane, tetracosane, and their mixtures	Materials Studio	COMPASS	The phase transition could be determined by the variation of self-diffusion coefficient and isobaric heat capacity
23	Yan Wang et al.[67]	2016	Water-paraffin (octadecane) mixtures	Not mentioned	COMPASS	Octadecane–water slurry simulations were performed to study the melting mechanism
24	Zeng and Khodadadi[68]	2018	n-Eicosane ($C_{20}H_{42}$) and n-triacontane ($C_{30}H_{62}$)	LAMMPS	NERD, LJ	The solid ratio plays a significant role in the thermal conductivity for low orientation factor systems
25	Luo and Lloyd[70]	2012	Paraffin ($C_{30}H_{62}$) containing graphene/graphite	Not mentioned	COMPASS[c], Airebo,[f69] LJ	Approaches to improve interfacial thermal transport are proposed
26	Babaei et al.[71]	2013	Paraffin (octadecane) containing graphene/CNT	LAMMPS	NERD[g], Tersoff, LJ	Introducing carbon nanotubes and graphene into long-chain paraffin leads to a considerable enhancement in thermal conductivity
27	Babaei et al.[72]	2013	Paraffin (octadecane) containing graphene/CNT	LAMMPS	NERD, Tersoff, LJ	The enhancement is higher for solid-phase mixtures
28	Babaei et al.[73]	2013	Paraffin (octadecane) containing graphite	LAMMPS	NERD, Tersoff, LJ	Solid interfaces have higher conductance concerning the liquid phase systems
29	Huang et al.[75]	2015	Paraffin (nonadecane) containing graphene/graphene oxide	Materials Studio	Universal force field (UFF)[74]	Non-covalently-functionalized graphene surfaces would indirectly affect thermal conductance
30	Yu Wang et al.[76]	2015	Paraffin ($C_{30}H_{62}$) containing doped graphene	LAMMPS	PCFF[b], Airebo, Tersoff, LJ	The hydrogenation of graphene exerts opposite effects on the properties of graphene–paraffin nanocomposites
31	Lin and Rao[77]	2016	Paraffin (eicosane) containing BNNS/BNNT	LAMMPS	TraPPE[h], Tersoff, LJ	The thermal conductivity of paraffin could be improved by boron nitride
32	Li et al.[78]	2017	Paraffin (octadecane) containing Cu nanoparticles	Materials Studio	COMPASS	Cu nanoparticles can improve the thermal properties of n-octadecane
33	Liu and Rao[79]	2017	Paraffin (octadecane) containing CNT on the copper surface	Materials Studio	COMPASS	Thermal diffusion and phase transition of C18H38 were investigated in detail
34	Yuan et al.[80]	2018	Paraffin (octadecane) containing pristine and functionalized graphene (by hydroxyl, carboxyl, and ethyl)	Materials Studio	COMPASS	The system functionalized by ethyl obtained a 10 K increase in phase change temperature

Table 1 (Contd.)

No.	Authors	Date	Simulated materials	Simulation software	Force fields	The main result
35	Yu et al.[81]	2019	Molten salt (NaCl) containing SiO_2 nanoparticles	Materials Studio, LAMMPS	COMPASS	The structural deformation during the phase transition of CPCM was observed
36	Zhang et al.[82]	2019	Paraffin (pentacosane)/ ethylene-vinyl acetate (EVA)/ graphene	Materials Studio	Universal force field (UFF)[74]	Excessive graphene in paraffin/EVA could lead to crystalline disorder
37	Zhao et al.[83]	2020	Paraffin (octadecane) containing CuO nanoparticle	LAMMPS	CHARMM, LJ	Significant melting enthalpy reduction was found in NPCMs
38	Tafrishi et al.[84]	2020	Paraffin (tetracosane) containing graphene/CNT	LAMMPS	PCFF, Tersoff, LJ	Graphene and CNT increase the thermal conductivity of the tetracosane
39	Tafrishi et al.[85]	2020	Paraffin (octadecane) containing graphene and BNNS	LAMMPS	PCFF, Airebo, Tersoff, LJ	The nanocomposite had a lower density change, more heat capacity, more thermal conductivity, and a lower diffusion coefficient
40	Tong et al.[86]	2020	n-Eicosane confined in graphene	LAMMPS	NERD for alkanes	The contact layers are harder to melt and easier to solidify compared with the main part of the systems
41	Wang et al.[87]	2020	Eicosane containing Ag, Cu, Al, and Fe	Not mentioned	COMPASS	The presence of nanoparticles leads to more eicosane molecular conformations tending from a linear state to a bent state
42	Liu and Rao[89]	2020	n-Octadecane with boron nitride layers	Not mentioned	Dreiding,[88] LJ	The effect of defects of BN modified with functional groups on ITC was studied
43	Zhao et al.[90]	2021	Paraffin (octadecane) containing CuO nanoparticle	LAMMPS	CHARMM, LJ	The existence of a nanolayer reduces phonon scattering and promotes heat transfer
44	Yu et al.[93]	2021	NaCl containing CNT	LAMMPS	Born–Mayer–Huggins (BMH) potential,[91,92] Airebo, LJ	The NaCl-SWCNT-based CPCM was proposed and designed by materials design strategy
45	Jamshideasli et al.[94]	2021	n-Octadecane containing graphene sheets	LAMMPS	NERD, Tersoff, LJ	The solid phase paraffin mixture exhibits higher ITC than the liquid phase
46	Gu et al.[95]	2021	Capric acid/ethylene-vinyl/ graphene	Not mentioned	Universal force field (UFF), COMPASS	CA/EVA/GR keeps high latent heat at a low dosage of GR, but GR up to 14.4 wt% results in a large reduction
47	Li et al.[96]	2021	n-Eicosane containing functionalized graphene (with epoxide and hydroxyl groups)	Materials Studio	COMPASS	Interfacial thermal resistance is reduced by functionalized graphene
48	Wu et al.[97]	2021	Paraffin ($C_{22}H_{46}$) containing boron nitride nano sheets	LAMMPS	NERD, LJ	TC of composites is controlled by TC of h-BN and ITR at $n \leq 15$ and by the aspect ratio of h-BN $n > 15$
49	Glova et al.[101]	2021	n-Eicosane containing asphaltene	LAMMPS, GROMACS	GAFF[98] and CHARMM36 (ref. 99 and 100)	Chemically modified asphaltenes can be used as thermal conductivity enhancers
50	Tiantian et al.[102]	2021	n-Octadecane near graphite layers	Not mentioned	COMPASS, LJ	The thermal conductivity of amorphous n-octadecane is about 2.5 times lower than that of crystal n-octadecane
51	Gao et al.[103]	2022	Palmitic acid-containing graphene	Materials Studio	COMPASS	Adding graphene to palmitic acid reduces the radius of gyration and increases thermal conductivity and capacity

Table 1 (Contd.)

No.	Authors	Date	Simulated materials	Simulation software	Force fields	The main result
52	Rao et al.[104]	2012	Paraffin (octadecane) with SiO_2 shell	Materials Studio	COMPASS	The nano-encapsulated phase change materials with free shells will increase the fluidity of core material
53	Rao et al.[105]	2013	Paraffin (octadecane) with SiO_2 shell in the water Paraffin containing Al nanoparticle	Materials Studio	COMPASS	The mobility of the nanoparticle-enhanced PCM decreased with the increase of the diameter of nanoparticles
54	Nie et al.[106]	2015	Paraffin (hexacosane) in the CNT	Materials Studio	COMPASS	Paraffin molecules exhibited an orderly structural distribution near the inner wall of the CNTs
55	Liu et al.[107]	2017	Octacosanoic, docosane, polystyrene	Materials Studio	COMPASS	The polystyrene weakened the diffusion and the thermal response of the system
56	Liu and Rao[108]	2019	Hypercrosslinked polyurethanes with water	Not mentioned	COMPASS, LJ	The effect of crosslinkers on heat and mass transfer properties was discussed
57	Abbaspour et al.[109]	2021	Octadecane and eicosane encapsulated in different CNTs	DL_POLY	OPLSAA, LJ	A longer CNT has a lower melting point than the normal CNT system
58	D. Feng et al.[110]	2019	Polyethylene glycol in the mesoporous silica MCM-41	LAMMPS	CVFF[i], PCFF, LJ	The PEG/MCM-41-NH_2 showed superior phase-change performance than PEG/MCM-41-OH.
59	Li et al.[111]	2021	Stearic acid, octadecanol, octadecylamine, and octadecane in CNT	Materials Studio	Universal force field (UFF)	The molecular interactions between C18-PCM molecules with different functional groups were studied systematically

[a] Lennard-Jones. [b] Polymer consistent force field. [c] Condensed-phase optimized molecular potentials for atomistic simulation studies. [d] Paul, Yoon, and Smith. [e] Large-scale atomic/molecular massively parallel simulator. [f] Adaptive intermolecular reactive empirical bond order. [g] Nath, Escobedo and de Pablo-revised. [h] Transferable potentials for phase equilibria. [i] Consistent valence force field.

nucleation and melting behavior of n-alkanes (normal alkanes); butane to dodecane. The n-alkane model consists of a linear chain of segments –CH_2–, with the terminal segments –CH_3.[38] They used Ryckaert and Bellemans potential[29] for alkanes (butane to dodecane) and Lennard-Jones potential (12–6) for interactions between the segments (chains). Berendsen coupling technique[112] was used to bring desired temperature and pressure. At first, they increased the temperature to reach the melted and amorphous phase of alkane and then decreased the temperature to crystalize that. Results showed that using too low temperatures for crystalizing the alkane (by fast quenching rate), would undercool the system and not reach a crystalized one. Also, when the lower temperature was too high, crystallization did not occur. Fig. 3 shows crystalized undecane ($C_{11}H_{24}$). The investigations showed that with increasing the alkane chain, the crystallization growth rate increases too, however, the researchers declared that the growth rate pertain to the nucleus size and therefore the simulated system size. For lower chain alkanes like butane, no crystallization was observed.

They calculated the melting and crystalizing temperatures of alkanes. The melting temperature was greater than the crystallizing temperature. The experimental melting temperature of alkanes was a value between the melting and crystallizing temperature. They also declared that since the boundaries were periodic, the heat needed for melting is more than a finite boundary, so leading to overheating.[113] Shimizu and Yamamoto[32] declared that the melting of n-decane ($C_{10}H_{22}$) is significantly affected by its state on the surface. They observed that the beginning of liquefying is in the inside of the film (Fig. 4).

Tsuchiya et al.[37] calculated the melting temperature of some n-alkanes using the resulted RDF (radial distribution function) curves. They used the PCFF force field and 6–9 Lennard-Jones for the van der Waals forces with the NPT ensemble.[114,115] Table 2 shows their calculated results of melting points and densities.

Zhen Li and Yamamoto[40] simulated the melting of n-nonadecane ($C_{19}H_{40}$) by the MD approach. They observed that in a temperature range of 385 K to 410 K, the center layer inclines to be in the liquid state with both surface layers staying crystalline. The surface monolayer particles showed huge translational vacillations along the chain axes. Mavrantza et al.[41]
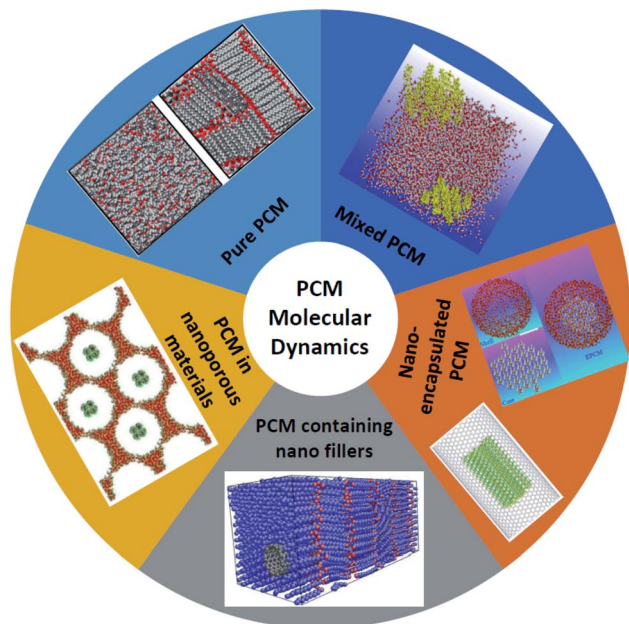
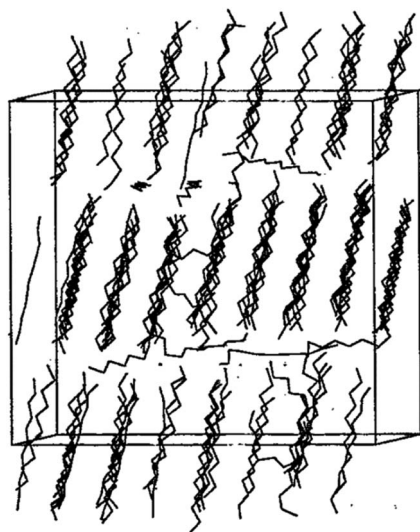Fig. 2 Classification of molecular dynamics of phase change materials.

Fig. 3 127 undecane chains in crystalline form (this figure has been reproduced from ref. 31 with permission from AIP Publishing, copyright 1981).

simulated some different chain numbers of polyethylene: $C_{14}H_{28}$, $C_{16}H_{32}$, $C_{23}H_{48}$, $C_{24}H_{48}$, $C_{48}H_{96}$, and $C_{96}H_{192}$. The study aimed to calculate the IR vibrational spectra of the orthorhombic phase of crystalline PE and studied *trans–gauche* defects. Bulk *n*-eicosane was simulated by Waheed *et al.*[43] using the PYS force field[42] and LJ. At first, the *n*-eicosane was warmed from 200 K to 500 K and then quenched to 285 K. Fig. 5 shows the quenching of *n*-eicosane. Crystallization fronts started at the two surfaces and advanced to the cell's focal point.

Marbeuf and Brown[45] simulated *n*-alkanes: $C_{18}H_{38}$, $C_{19}H_{40}$, and $C_{20}H_{42}$. Using DL-POLY software,[44] 600 molecules were simulated.
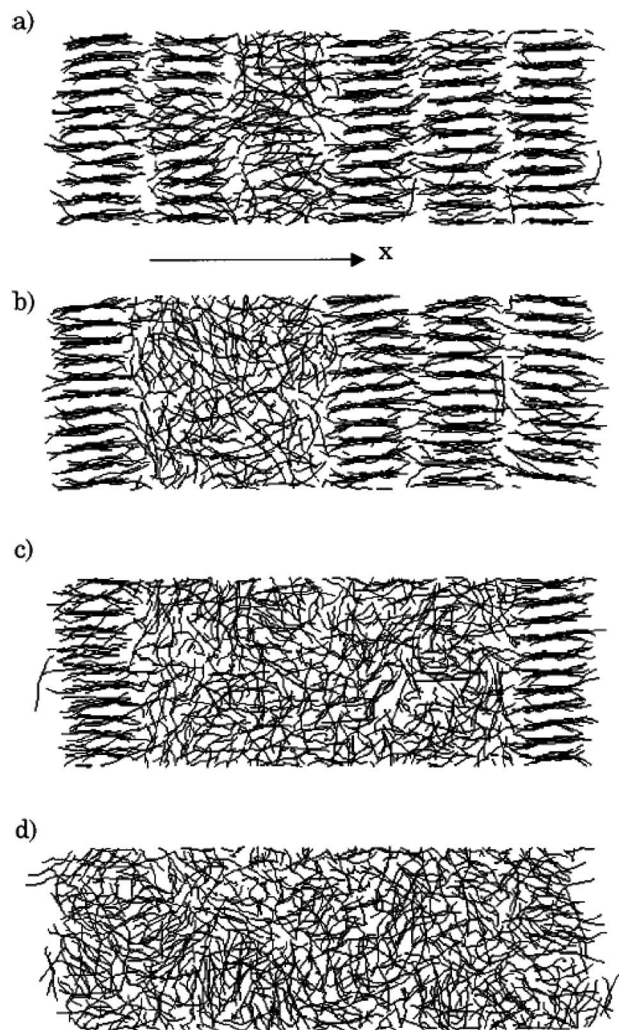
Fig. 4 Molecular trajectory during liquefying at 324 K (this figure has been reproduced from ref. 32 with permission from AIP Publishing, copyright 2000).

Diama *et al.*[47] simulated tetracosane (n-$C_{24}H_{50}$) and dotriacontane (n-$C_{32}H_{66}$) adsorption on a graphite surface. They used Weber[46] and LJ potentials. Fig. 6 shows snapshots of the simulation of the $C_{24}H_{50}$ monolayer. At lower densities, most of the molecules are arranged parallel to the surface of the graphite. However, at the highest densities, some molecules are moved around.

Jayaraman *et al.*[49] used nonequilibrium MD simulation to calculate viscosities, thermal conductivities, thermal capacities, and melting points of nitrate salts ($LiNO_3$, $NaNO_3$, KNO_3) with LAMMPS software.[48] The used potential and time step were Buckingham and 1 fs respectively. The *ab initio* calculations for heat capacity calculation were carried out using Gaussian. Fig. 7 shows the simulated $LiNO_3$ structure. It turned out that the exact melting point was a very sensitive test of the force field accuracy. Table 3 represents some results of this research.

The nucleation of *n*-eicosane crystals was studied by Yi and Rutledge.[50] The molecular dynamics system was composed of 336 *n*-eicosane molecules. The force field was PYS[42] parameterized using reference.[116] They fitted the curve of free energy to

Table 2 Calculated melting range and densities of some *n*-alkanes reproduced with permission from ref. 37

Name	Molecular formula	Calculated melting range (K)	Calculated density (g cm^{-3}) in 240, 260, and 280 K respectively
n-Octane	*n*-C$_8$H$_{18}$	200–210	0.7555, 0.7266, 0.6140
n-Decane	*n*-C$_{10}$H$_{22}$	210–220	0.7720, 0.7401, 0.6657
n-Dodecane	*n*-C$_{12}$H$_{26}$	240–250	NM^a, 0.7767, 0.7602
n-Tetradecane	*n*-C$_{14}$H$_{30}$	260–270	NM, nm, 0.7804
n-Hexadecane	*n*-C$_{16}$H$_{34}$	250–260	NM, nm, NM

^{a} Not mentioned.

the model of the cylindrical nucleus. Interfacial free energies were determined to be 10 mJ m^{-2} and 4 mJ m^{-2} for the side surface and the end surface, respectively.
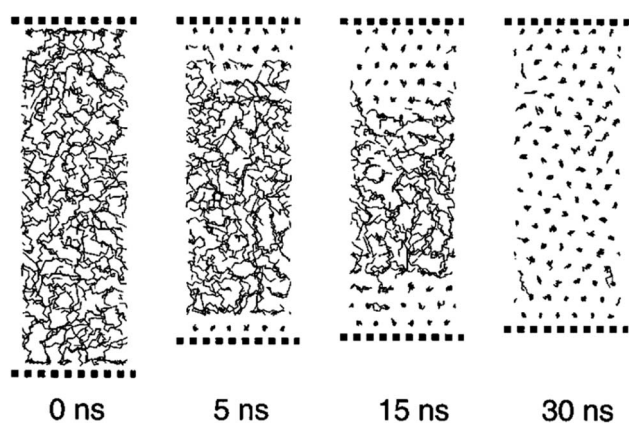
Fig. 5 Quenching of *n*-eicosane from melt phase to solid phase (this figure has been reproduced from ref. 43 with permission from AIP Publishing, copyright 2002).
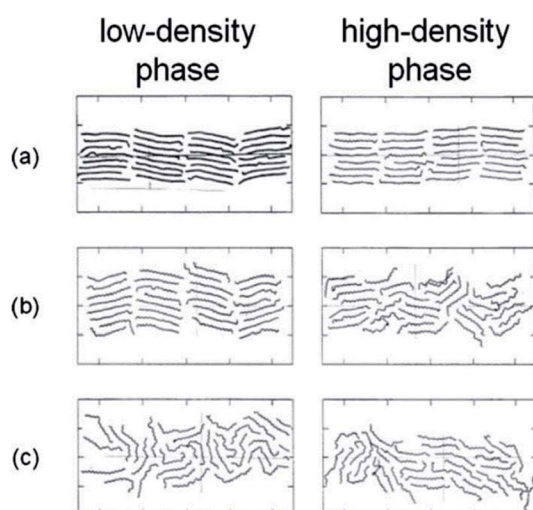
Fig. 6 Snapshots showing top views of the MD simulated cells of lower-density (left) and higher-density (right) C$_{24}$H$_{50}$ at different temperatures: (a) 300 K, (b) 325 K, and (c) 350 K (this figure has been reproduced from ref. 47 with permission from AIP Publishing, copyright 2009).

Rao *et al.*[51] investigated *n*-nonadecane PCM (C$_{19}$H$_{40}$) phase transition under high pressure. By using the Materials Studio 5.5 software[117] the simulations were carried out. Fig. 8 shows the simulation system of *n*-nonadecane PCM. As a result, it was found that the melting temperature of *n*-nonadecane at high pressure was greater than the melting temperature at atmospheric pressure, and the *n*-nonadecane order parameter decreased as the temperature increased.

Andersen's method[115] was used for temperature control and Berendsen method[112] for pressure control. The Verlet velocity algorithm[118,119] was used to integrate the motion equation. The melting and solidification temperatures of *n*-nonadecane were about 323 K. The simulated melting temperature was greater than that of atmospheric pressure because it suppressed the high-pressure chain turning and molecular motion. As the temperature raised, the peak of the radial distribution function (RDF) weakened, indicating that the nonadecane order parameter decreased.

Rastgarkafshgarkolaei *et al.*[53] simulated paraffin: C$_{20}$H$_{42}$, C$_{24}$H$_{50}$, C$_{26}$H$_{54}$, and C$_{30}$H$_{62}$ molecules. Using NEMD (non-
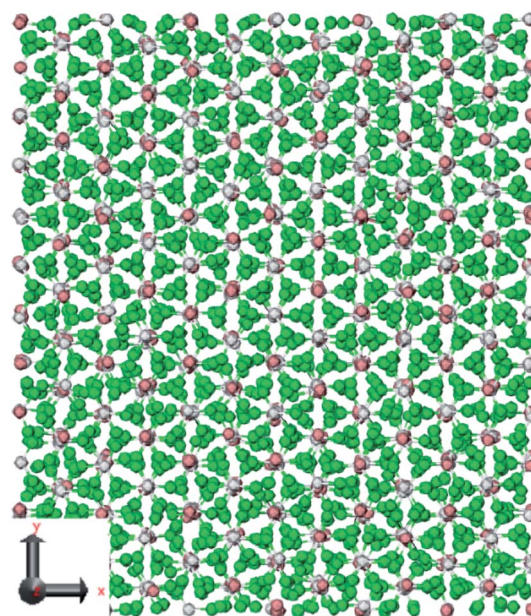

Fig. 7 Crystal structures of LiNO$_3$. The green atoms depict oxygen, the gray atoms depict nitrogen, and the pink atoms depict lithium (this figure has been reproduced from ref. 49 with permission from ACS, copyright 2009).

© 2022 The Author(s). Published by the Royal Society of Chemistry

Table 3 Calculated parameters from ref. 49, reproduced with permission

Nitrate salt	Calculated melting point (K)	Calculated thermal conductivity (W mK^{-1})	Calculated viscosity (centipoise)	Calculated density (g cm^{-3})
LiNO$_3$	459 $\pm$ 10	0.69	1.5	1.691
NaNO$_3$	591 $\pm$ 18	0.58	1.75	1.7397
KNO$_3$	513 $\pm$ 17	0.51	1.62	1.688

equilibrium molecular dynamics) and EMD (equilibrium molecular dynamics), researchers calculated the thermal boundary conduction between the ideal crystals of paraffin layers. No significant change was observed in thermal conductance in molecular length. The thermal conductivity of three phases of paraffin (solid, liquid, and ideal crystal) was calculated using the NEMD method. The force field was NERD (Nath, Escobedo, and de Pablo revised[52]). Fig. 9 a displays C$_{20}$H$_{42}$ molecules in the ideal crystal form. For creating liquid structures, the systems were equilibrated at 360 K. Subsequently, by cooling the system to 230 K, solid structures were built. The liquid and the solid structures of *n*-eicosane can be seen in Fig. 9b and c.

NEMD method was used in the thermal conductivity calculation simulations. Heat flux was imposed over the structure by interchanging thermal energy between the cold and hot regions (Fig. 9d). Temperatures of each region (of the length of imposed heat) were recorded, after reaching the steady-state. Then, using Fourier's law, the thermal conductivity was calculated. The related Fourier's law formula is as follows:

$$q_x = -k\frac{\mathrm{d}T}{\mathrm{d}x} \tag{2}$$

where k is the thermal conductivity and $\frac{\mathrm{d}T}{\mathrm{d}x}$ is the temperature gradient in the x-direction (the direction of thermal energy was imposed). Results showed that as the number of carbon atoms increases, the thermal conductivity increases slightly. On the other hand, with increasing the alignment of the molecules, the

thermal conductivity increases significantly. The ideal crystal showed the highest thermal conductivity, because of the highest ordered structure.

Ni *et al.*[54] studied molten nitrate salts LiNO$_3$, NaNO$_3$, and KNO$_3$. They calculated the density, thermal conductivity, heat capacity, and viscosity of the salts. Simulations were carried out using the Buckingham force field. Researchers expressed that the molten salt maintains some crystal structure at high temperatures. The LiNO$_3$ coordination was a pentacoordinate structure. While the NaNO$_3$ and KNO$_3$ showed a hex coordinate structure. Fig. 10 shows the calculated viscosities with EMD and NEMD methods.

Two methods were utilized for calculating the heat capacity, the energy fluctuation method and the enthalpy method (Table 4). Researchers also simulated a mixture of KNO$_3$ and NaNO$_3$. They proposed that the used force field and methods of simulations can be advanced. In the future, there is a need of simulating more complex molten salts and their mixtures.

Cui *et al.*[55] simulated NaCl and KCl as salt PCMs, using EIM potential. Two methods of heat flux and the Muller–Plathe method were utilized to calculate the thermal conductivity. They have also investigated binary NaCl–KCl systems. Melting transition was indicated by density drop (at higher temperatures). Researchers concluded that the EIM potential could not be appropriate to calculate NaCl and KCl melting points precisely. The thermal expansion coefficients for NaCl and KCl, calculated from the slope of the ln(volume)–temperature line, were 3.561 $\times$ 10^{-5} K^{-1} and 3.462 $\times$ 10^{-5} K^{-1}, respectively. According to Fourier's law, the calculated thermal conductivity using the heat flux method (NEMD) for NaCl was 3.317 W mK^{-1} and for KCl was 1.776 W mK^{-1}. Also, the calculated thermal conductivities using the Muller–Plathe method (EMD) for NaCl and KCl were 2.713 and 1.396 W mK^{-1}, respectively.

B. Feng *et al.*[57] simulated pentaerythritol (a solid–solid PCM) to calculate its thermal conductivity. Pentaerythritol has a latent heat of ~280 kJ kg^{-1} and the temperature of its solid–solid phase transition is ~459 K.[120,121] Pentaerythritol crystals absorb heat and transform from BCT† structure (the α phase) to FCC‡ structure (the γ phase) accompanied by a large amount of thermal energy storage (Fig. 11). During the process of releasing thermal energy, γ phase pentaerythritol can transform back to the α phase.[122] Researchers used non-equilibrium MD simulations using the GROMOS[56] force field to clarify the relationship between thermal conductivity and crystalline structures of pentaerythritol.
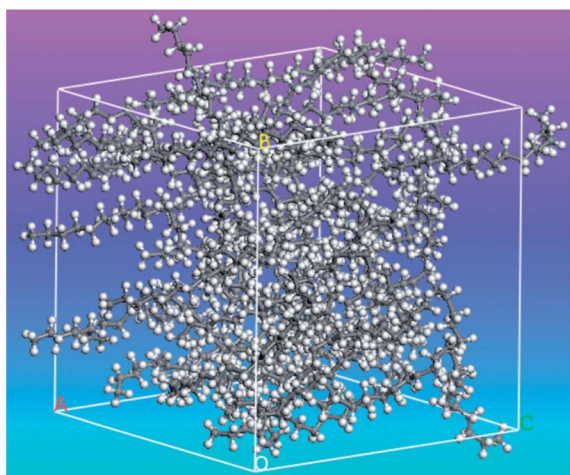

Fig. 8 The simulated amorphous structure of *n*-nonadecane (this figure has been reproduced from ref. 51 with permission from Taylor & Francis, copyright 2012).

† Body-centered tetragonal.
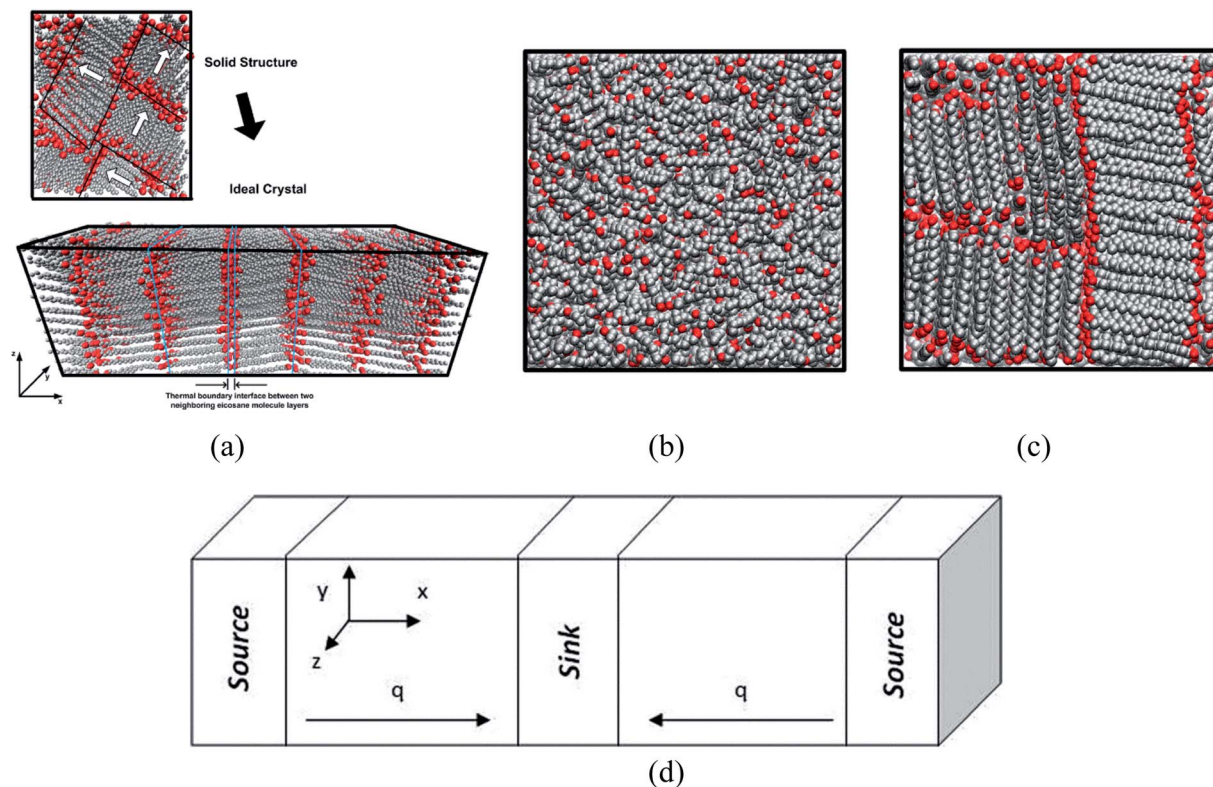
‡ Face-centered cubic.

Fig. 9 (a) Ideal crystal of $C_{20}H_{42}$ molecules (grey and red spheres display $-CH_2-$ and $-CH_3$, respectively). n-Eicosane molecules in (b) the liquid phase and (c) the solid phase. (d) The simulation box and the configuration of thermal energy sources and sink (This figure has been adapted from ref. 53 with permission from AIP Publishing, copyright 2016).
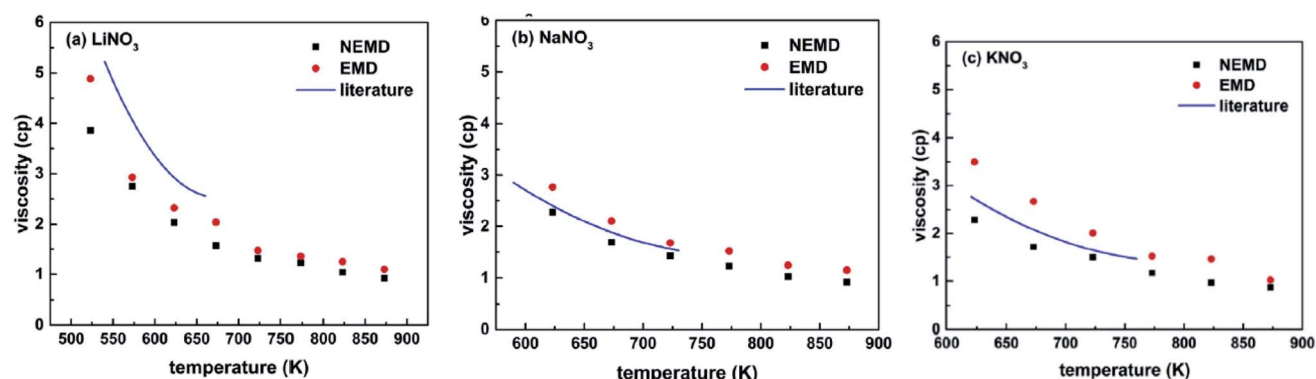

Fig. 10 The calculated viscosities of nitrate salts (a) $LiNO_3$; (b) $NaNO_3$; (c) KNO_3 (this figure has been adapted from ref. 54 with permission from Elsevier, copyright 2019).

Results showed that by increasing the temperature from 303 K to 453 K, the thermal conductivity diminished from 0.66 W mK^{-1} to 0.53 W mK^{-1}. When the temperature of pentaerythritol was higher than $T_{\alpha\gamma}$, the thermal conductivity diminished remarkably to 0.23 W mK^{-1}. By further increasing of temperature, the thermal conductivity decreased to 0.20 W mK^{-1}. The degradation and weakening of hydrogen bonds after the transition from α to γ phase could be the most important change in crystal structures, leading to the halving of the thermal conductivity of pentaerythritol.

Octadecanoic acid is an excellent PCM due to its narrow phase change temperature and high energy density. Y. Feng *et al.*[59] studied octadecanoic acid with EMD simulations for investigating the thermal conductivity size-dependency of bulk, nanowire, and nanochain forms of octadecanoic acid. The time step was set to 0.1 fs because of the high-frequency vibrations of hydrogen atoms. The simulations were implemented using the CHARMM force field in the LAMMPS package. At first, the octadecanoic acid relaxed at the temperature of 300 K under the NVT ensemble for 0.1 ns. Then under the NVE ensemble (for 1

Table 4 Calculated heat capacities of nitrate salts (J kg^{-1} K^{-1}) (this table has been adapted from ref. 54 with permission from Elsevier, copyright 2019)

Method	LiNO$_3$	NaNO$_3$	KNO$_3$
Energy fluctuation	2200.8	1636.7	1605.6
Enthalpy	2183.6	1770.6	1486.2

ns), the heat flux was simulated. Switching the NVT to the NVE ensemble was for obtaining a more stable heat flux. Bulk, nanowire, and nanochain forms of octadecanoic acid had thermal conductivities of 0.45, 0.20, and 0.001 W mK^{-1}, respectively. For investigating the size effect of thermal conductivity, the VDOS (vibrational density of states) and phonon overlap energy were compared. The nanowire form had lower thermal conductivity compared to the bulk form because the limited size of the nanowire geometry reduces the vibrations of the atoms and weakens the phonon matching level. The nanochain form of the octadecanoic acid has a curled structure, so it shows higher molecular distances and more phonon scattering probabilities under weak van der Waals forces that lead to the reduction of thermal transportation.

Feng *et al.*[60] studied the monohydric alcohols C$_{12}$H$_{26}$O, C$_{14}$H$_{30}$O, and C$_{16}$H$_{34}$O. By imposing tensile strains on ideal crystals of monohydric alcohols, the intrinsic thermal conductivity was enhanced. GROMOS and LJ potential were utilized in the simulations. The ideal crystal models of monohydric alcohols showed a higher thermal conductivity than their original ones. When the applied tensile strain was 0.1, the thermal conductivities increased by 170%. So, the main result of this research was that by imposing certain tensile strains (on nanomaterials with highly ordered structures), their heat transfer performance enhances. In another similar research, Feng *et al.*[61] calculated the thermal conductivity of C$_{12}$H$_{26}$O, C$_{14}$H$_{30}$O, and C$_{16}$H$_{34}$O. The ideal crystals had twice the amount of thermal conductivity compared to the solid samples. The predicted thermal conductivity of the ideal crystal of C$_{16}$H$_{34}$O reached up to about 0.449 W mK^{-1}, while that of the solid C$_{16}$H$_{34}$O was only about 0.218 W mK^{-1}. Also, when the interfaces of these monohydric alcohols are surrounded by –OH groups, the interfacial thermal transfer coefficient will be fourfold larger than those surrounded by –CH$_3$ groups.

3.2 Simulations of mixed PCMs with each other (slurry PCMs)

Molecular dynamics studies of mixtures and slurry PCMs will discuss in this section. Wentzel and Milner[64] studied the simulation of pure C$_{23}$H$_{48}$ alkane and the mixture of C$_{21}$H$_{44}$ and C$_{23}$H$_{48}$. They used OPLSAA[62] and flexible Williams[63] force fields. But only the flexible Williams force field gave good agreement with the experimental results. Rao *et al.*[65] investigated the molecular dynamics simulating water and *n*-nonadecane paraffin (C$_{19}$H$_{40}$) mixtures. They constructed the mixtures with
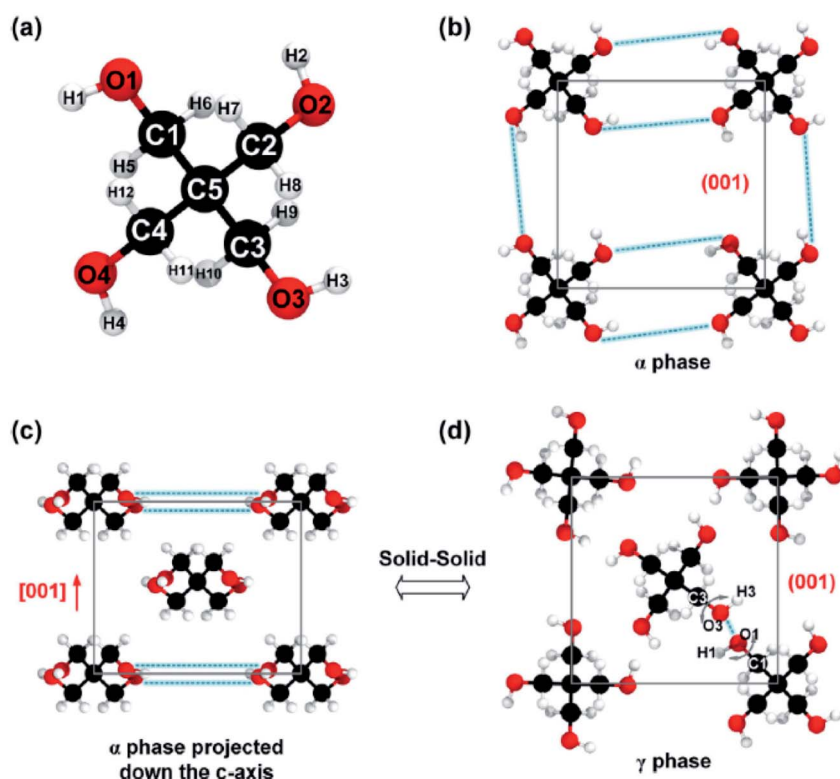

Fig. 11 (a) Arrangement of atoms of a single pentaerythritol molecule, (b) pentaerythritol BCT structure, (c) FCC crystalline structure of pentaerythritol, and (d) FCC crystalline structure of pentaerythritol with intermolecular bond rotation (this figure has been reproduced from ref. 57 with permission from Elsevier, copyright 2019).
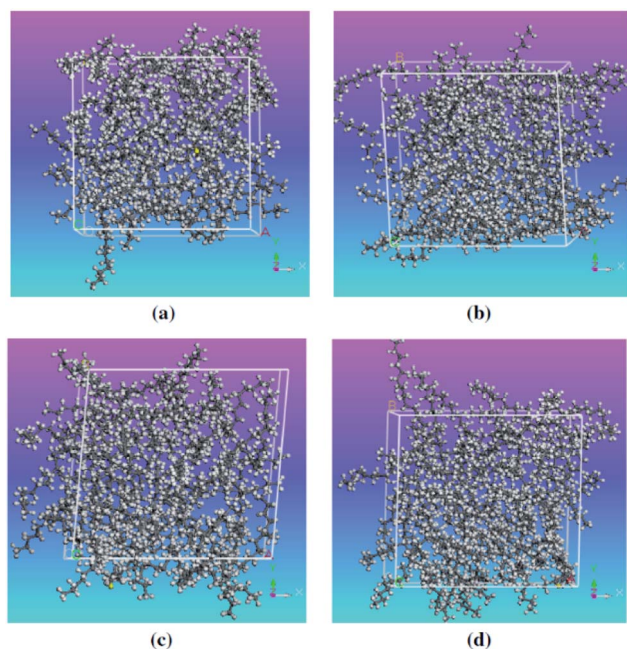
Fig. 12 Construction of PCM mixtures: (a) pure nonadecane; (b) pure tetracosane; (c) mixture of nonadecane and tetracosane, 1/1; (d) mixture of nonadecane and tetracosane, 3/1 (this figure has been reproduced from ref. 66 with permission from Elsevier, copyright 2013).

different paraffin mass fractions (0%, 10%, 20%, and 30%). Simulations were carried out using the COMPASS force field, a cutoff distance of 9.5 Å, and a time step of 1 fs. The Berendsen[52] and Andersen[115] methods were utilized to control the pressure and the temperature, respectively. Materials Studio software (Accelrys)[117] was used for the MD simulations. The mixtures' self-diffusion coefficient was enhanced with temperature increasing but diminished with increasing the nonadecane mass fraction. Despite decreasing mobility because of mixing paraffin into the water, the thermal energy storage capacity increased. In another study, nonadecane ($C_{19}H_{40}$), tetracosane ($C_{24}H_{50}$), and their mixtures were simulated by Rao *et al.*[66] As shown in Fig. 12, they constructed four PCM mixtures with different proportions of different kinds of paraffin (pure nonadecane, pure tetracosane, equal molar

fraction of nonadecane, and tetracosane, nonadecane triple of tetracosane).

The mean square displacement (MSD), which means measuring the mean range of all particles over time, is commonly used to define the system conduct in phase changes. Eqn (2) was used to compute the MSD:

$$\text{MSD} = \frac{1}{N}|r_i(t) - r_i(0)|^2 \qquad (3)$$

where N is the number of atoms and r is the position of the atoms in angstrom units. $r_i(t)$ is the position of the i-th atom in the time step of t.

Based on the Einstein equation,[123] the self-diffusion coefficient (D) was computed as follows:

$$D = \frac{1}{6N} \lim_{t \to \infty} \frac{\mathrm{d}}{\mathrm{d}t} \sum_{i=j} N|r_i(t) - r_i(0)|^2 \qquad (4)$$

where the angular brackets define the ensemble's average. The value of the self-diffusion coefficient was computed using the MSD curve slope. The melting point of the PCM mixture can be predicted by the diffusion coefficient and the MSD curve. Results showed that pure *n*-nonadecane and pure *n*-tetracosane systems melted in 307.4 K and 324.6 K, respectively. The melting points of the mixtures were 308.5 K and 315.2 K for nonadecane-tetracosane, 1/1, and nonadecane-tetracosane, 3/1, respectively. Also, the peaks of radial distribution functions (RDF) of the PCM systems became wider and weaker after melting. This means that with increasing the temperature, the mobility of alkane molecules increases too. Yan Wang *et al.*[67] simulated pure octadecane and water–octadecane mixtures. The melting point was determined using the relationship between the potential energy of octadecane and its temperature. Fig. 13 shows the structures of simulated systems.

The potential energy *versus* temperature curve showed that the melting range of octadecane is between 295 K and 305 K. This result is close to the experimental results. Also, they demonstrated that by enhancing the octadecane mass fraction in the mixtures, the heat capacity of the mixture diminished. Maybe this was due to the higher heat capacity of water, that with increasing the paraffin mass fraction, the mass fraction of water decreases and so decreases the heat capacity of the mixture.
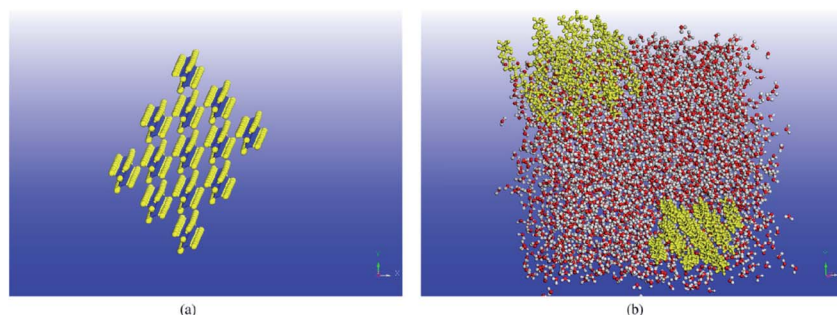

Fig. 13 The constructions of (a) pure octadecane and (b) octadecane–water mixture (this figure has been reproduced from ref. 67 with permission from Elsevier, copyright 2016).

The mechanism of paraffin mixtures crystallization was studied by Zeng and Khodadadi.[68] They simulated the n-eicosane ($C_{20}H_{42}$) and n-triacontane ($C_{30}H_{62}$) with different mass fractions. Results showed a great influence of the orientation factor of paraffin molecules on the thermal transport properties of the mixtures. The mass fraction of n-triacontane had a negligible impact on the thermal transport properties of the mixtures. Moreover, results showed that the solid ratio plays a significant role in the mixtures' thermal conductivity with low orientation factors.

3.3 Nano-enhanced PCM simulations

Molecular dynamics studies of nanocomposite PCMs which mean PCM incorporating nano-additives will discuss in this section. Luo and Lloyd[70] investigated the interfacial thermal conductance of graphene/graphite–paraffin. They used Airebo potential[69] for graphene and graphite, COMPASS for $C_{30}H_{62}$, and LJ (Lennard-Jones) for interactions between them. The cutoff radius of LJ was 10 Å and the time step was 0.25 fs. They heated and cooled the structures several times to release internal uneven stresses. Then by using the NPT ensemble, the structures reached their optimized size (equilibration step). Then they used non-equilibrium molecular dynamics (NEMD) by allocating two 5 Å thick regions for the heat source and sink. They fixed a thin region in each turn of the long box and then defined the heat slabs (source and sink) near them. The thermal conductance (G) was calculated by using $G = J/\Delta T$ formula. In this formula, J is the heat flux and ΔT is the temperature difference of interface material (temperature discontinuity of two sides of graphene/graphite). Thermal conductance was calculated over 2 000 000 time steps (0.5 ns). The thermal conductivity of pure paraffin was obtained at 0.327 W mK^{-1} (the related temperature of this calculation is not mentioned in the paper, but it was probably at 300 K). Firstly, they studied the effect of simulation box size on the thermal conductance of paraffin and resulted in no obvious size dependency. This was concluded that in paraffin because of short bond lengths, major phonons (heat carriers) have very short propagation lengths. But for graphene–paraffin mixtures size dependency, the research showed that phonons with a wave length larger than about 20 Å contribute 15% to thermal conductance. Besides phonons with a wave length larger than about 40 Å contribute only 7% to the thermal conductance results. They declared that graphene–paraffin thermal conductance (61–71 MW m^{-2} K^{-1}) is more than that of CNT–paraffin. But they referenced a study for CNT–argon thermal conductance[124] that was 1–3 MW m^{-2} K^{-1}. Also, researchers had found that by changing the van der Waals interactions between paraffin and graphite to covalent bonds, the interfacial thermal conductance will increase to about 536 MW m^{-2} K^{-1} (Fig. 14). This is because of the higher energy of covalent bonds rather than van der Waals ones.

They also found that graphene–paraffin thermal conductance is higher than that of graphite–paraffin, because of higher carbon atoms per unit area of graphene (0.38 atom per Å^2) rather than graphite (0.12 atom per Å^2). Furthermore, they found that when van der Waals interactions between paraffin
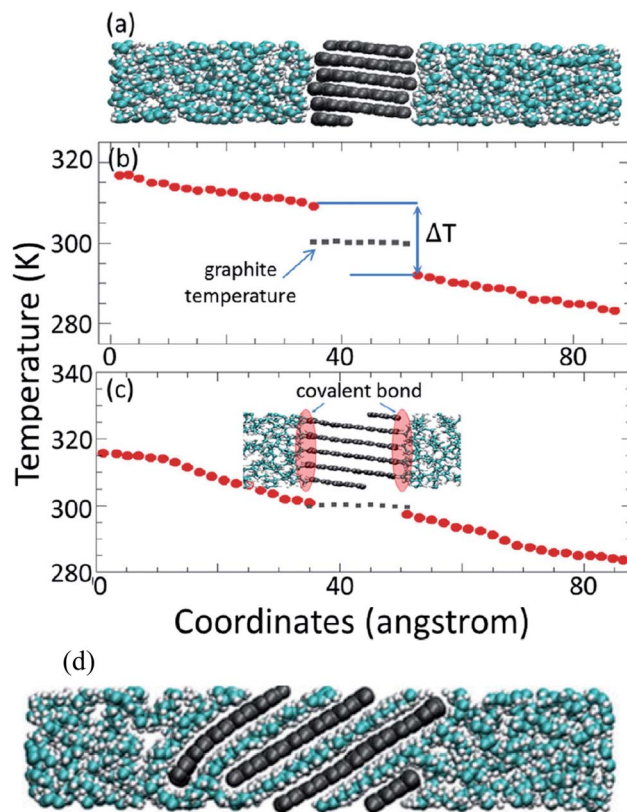

Fig. 14 (a) Paraffin–graphite structure with van der Waals interaction. (b) Paraffin–graphite thermal conductance using the NEMD method. (c) Paraffin–graphite structure with covalent bonds between edge atoms of graphite and paraffin molecules that result in higher thermal conductance. (d) Graphite exfoliation by paraffin molecules in the condition of high energy van der Waals interactions (this figure has been adapted/reproduced from ref. 70 with permission from Wiley Publications, copyright 2012).

and graphite become more than three times, the paraffin molecules will penetrate between graphite flakes and will exfoliate it into single graphene sheets (Fig. 14d). The authors also investigated the impact of density on graphene–paraffin thermal conductance. They increased the density of paraffin (by increasing the pressure) from 0.7 to 0.89 g cm^{-3} and saw that thermal conductance increases monotonically. This was because of the interactions of more paraffin atoms with graphene. Because the RDF§ diagram of the graphene–paraffin mixture showed higher peaks with increasing density and so this can confirm the previous sentence. Furthermore, with density rising, the peaks of vibration power spectra shifted from lower frequencies to higher ones.

Babaei et al.[71] utilized nonequilibrium MD simulations to study the relationship between the octadecane paraffin structure and its thermal conductivity. Using NERD force field and a time step of 1 fs, they simulated octadecane, octadecane–graphene, and octadecane–CNT nanocomposites. CNT and graphene were kept fixed after the equilibration of the systems.
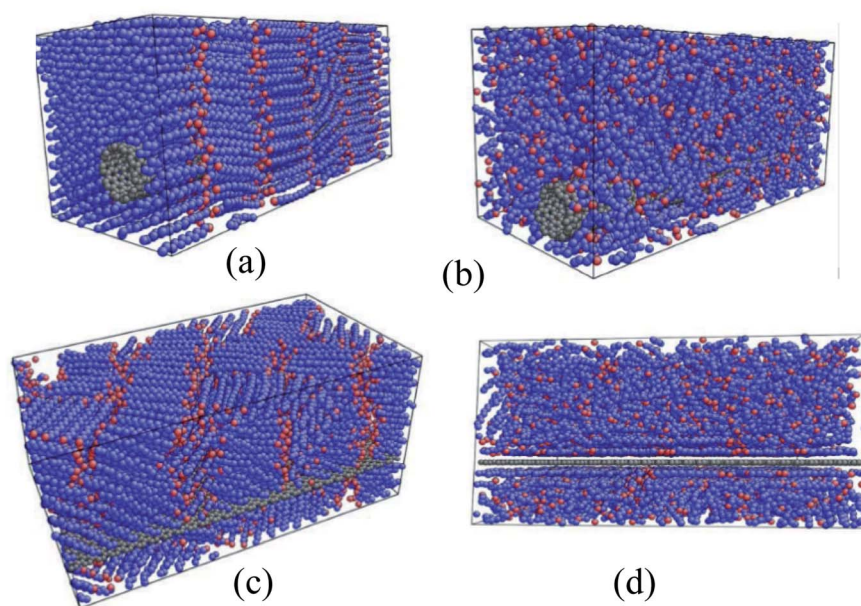
§ Radial distribution function.

Fig. 15 (a) Solid and (b) liquid octadecane–CNT mixtures. Octadecane–graphene mixtures in (c) solid state and (d) liquid state (this figure has been adapted from ref. 71 with permission from Elsevier, copyright 2013).

Researchers declared that this method allows the simulations to calculate just the paraffin's thermal conductivity. LAMMPS package was used for doing the simulations. Results showed that with the crystallization of pure paraffin, the thermal conductivity raised, and in the composites, the ordering of paraffin molecules increased, which resulted in a higher thermal conductivity in liquid structures in comparison with liquid pure paraffin. Researchers concluded that this increase in thermal conductivity is due to both the higher thermal conductivity of the fillers and the filler-induced alignment of paraffin molecules. Fig. 15 shows the octadecane–CNT and octadecane–graphene nanocomposites in the solid and liquid phases (crystallized and amorph shapes).

The parameter of molecular alignment, s, is calculated as follows:[125]

$$s = \left| \frac{\langle \cos^2 \theta \rangle - 1/3}{2/3} \right| \tag{5}$$

where θ is the molecules' end-to-end vector angle and the desired axis, with $\langle\langle$ represents the average value acquired on all molecules. The arrangement parameter varies from 0 to 1 corresponding to the completely random orientation of the molecules and the perfectly arranged molecules, respectively. The thermal conductivity and molecular alignment results are reported in Table 5. The result that the solid composite obtained a greater enhancement of thermal conductivity was due to remarkable ordering caused by directional crystallization.

Babaei *et al.*[72] studied again the effect of adding graphene and CNT to octadecane paraffin. The average value of thermal conductivity of octadecane–graphene and octadecane–CNT liquid mixtures was about 0.21 W mK^{-1}. While the solid octadecane–CNT nanocomposite was about 0.5 W mK^{-1}. So, the results of octadecane–CNT nanocomposite showed an improvement of 68% in comparison with pure paraffin. Researchers concluded that the more-ordered paraffin molecules exhibited enhanced thermal conductivity. In another investigation, Babaei *et al.*[73] studied graphene and paraffin interfacial thermal conductance. They constructed graphene with different layer numbers. Solid paraffin showed higher interfacial thermal conductance in comparison with the liquid

Table 5 Thermal conductivity results and alignment parameter values of pure octadecane, octadecane–graphene mixture, and octadecane–CNT mixtures (this table has been adapted from ref. 71 with permission from Elsevier, copyright 2013)

| Material	Phase	Temperature	Thermal conductivity	Alignment parameter
Pure octadecane paraffin	Liquid	300 K	0.164 W mK^{-1}	0.02
Pure octadecane paraffin	Solid	270 K	0.30 W mK^{-1}	0.15
Pure octadecane paraffin	Perfect crystal along with the molecules	270 K	1.126 W mK^{-1}	0.987
Pure octadecane paraffin	Perfect crystal perpendicular	270 K	0.347 W mK^{-1}	Not mentioned
Octadecane–CNT nanocomposite	Liquid	300 K	0.243 W mK^{-1}	0.11
Octadecane–CNT nanocomposite	Solid	270 K	0.499 W mK^{-1}	0.908
Octadecane–graphene nanocomposite	Liquid	320 K	0.249 W mK^{-1}	0.20
Octadecane–graphene nanocomposite	Solid	270 K	0.560 W mK^{-1}	0.28
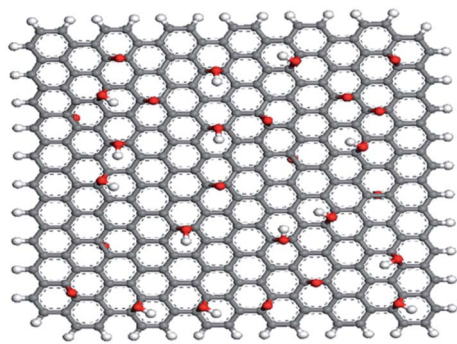
Fig. 16 Structure of graphene oxide. The white and red colors are for H and O atoms, respectively (this figure has been adapted from ref. 75 with permission from Elsevier, copyright 2015).

one. Also, by increasing the graphene layer number, the interfacial thermal conductance diminished in both liquid and solid states.

Huang et al.[75] simulated pure paraffin, paraffin–graphene mixture, and paraffin–graphene oxide mixture. The selected paraffin was n-nonadecane with a molecular formula of $C_{19}H_{40}$. The graphene was a square shape with about 2.5 nm side with H-terminated edges while graphene oxide contained 14 hydroxyl and 14 epoxy groups. Fig. 16 shows the structure of constructed graphene oxide. The paraffin–graphene system possessed 3 graphene sheets and the paraffin–graphene oxide system contained 3 graphene oxides. Simulations were carried out using the UNIVERSAL force field,[74] under the NVT ensemble.

To ascertain the thermal conductivity of the systems, they used non-equilibrium molecular dynamics by imposing a heat flux in the system. Utilizing Fourier's law, the thermal conductivities were determined. Table 6 shows the results of thermal conductivities, diffusion coefficients, and heat capacities, of three simulated systems.

Researchers concluded that both graphene and graphene oxide nano additives can enhance the thermal conductivity and heat capacity of paraffin, but graphene oxide performed more efficiently than graphene.

Yu Wang et al.[76] concentrated on the mechanical and thermal properties of paraffin ($C_{30}H_{62}$) containing doped graphene. They focused on the change of paraffin–graphene interfacial thermal transport by utilizing different treatment strategies. They studied the effectiveness of hydrogenation, defecting, and doping in decreasing the paraffin–graphene interfacial thermal resistance. From the consequences of the

simulations of the paraffin–graphene mixtures under tensile loading, lower Young's modulus and smaller tensile strength were considered for the paraffin filled with hydrogenated graphene. Paraffin was simulated using the PCFF force field. For modeling the pristine and hydrogenated graphene, AIREBO potential was utilized.[126] For modeling the dopant atoms (boron and nitrogen), the Tersoff potential was used.[127,128] The Muller–Plathe method was adopted to investigate thermal transport behaviors. The time step was set to 0.25 fs. As displayed in Fig. 17a, the heat sink and source were situated at both ends and in the center of the composite model, respectively. The temperature gradient was set up between the heat sink and source (Fig. 17b). Between the heat source and sink regions, a heat flux (J) was applied under the NVE ensemble. A temperature jump ΔT at the interface of paraffin–graphene was observed. Interfacial thermal resistance R_K of the paraffin–graphene nanocomposite was calculated by:

$$R_K = \frac{\Delta T}{J} \tag{6}$$

The thermal conductivity of pure paraffin was 0.309 W mK^{-1}. Based on eqn (6), the paraffin–graphene interfacial thermal resistance was $R_{K0} = 0.669 \times 10^{-8}$ m^2 K^{-1} W^{-1}. With a 4.17% H-coverage, the interfacial thermal resistance between paraffin and graphene was reduced significantly by 11.6%. As shown in Fig. 20c, a tensile loading was applied with a strain rate of 0.0005 ps^{-1}, in the armchair direction. Stress–strain curves of the nanocomposites are plotted in Fig. 17d. Young's modulus and ultimate tensile strength of paraffin–graphene nanocomposite were 26.7 GPa and 2.85 GPa, respectively. The 4.17% hydrogenated graphene. A 4.17% hydrogenated graphene caused ~21% and ~9% deteriorations in the tensile strength and Young's modulus of the graphene–paraffin nanocomposites, respectively. Researchers expressed that: "hydrogenation of graphene triggers the transition of strong sp^2 bonds to weaker sp^3 bonds". Analysts concluded that with hydrogenating the paraffin–graphene nanocomposite, interfacial thermal conductance improves. But, this should be utilized wisely to minimize the reduction of its mechanical strength.

Lin and Rao[77] studied the effects of adding boron nitride nanosheet (BNNS) and also boron nitride nanotube (BNNT) to n-eicosane on its thermal properties. The structure of BNNS is analogous to graphene (hexagonal honeycomblike lattice) and has significant thermal conductivity. BNNT is similar to CNT and has high thermal conductivity either. They used LAMMPS for simulations and the used force fields were TraPPE (for

Table 6 Thermal conductivity, diffusion coefficient, and heat capacity value (this table has been reproduced from ref. 75 with permission from Elsevier, copyright 2015)

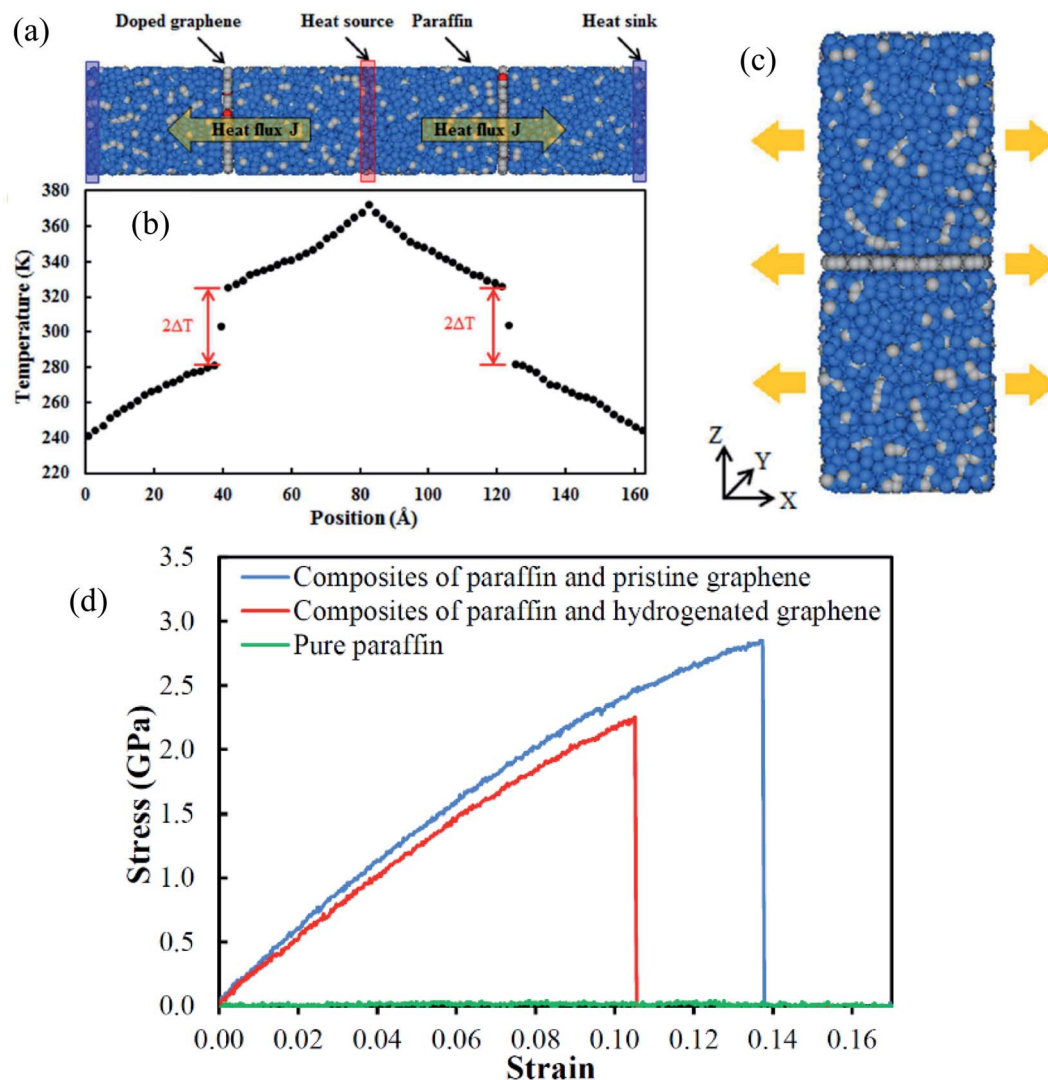|	Paraffin	Paraffin–graphene	Paraffin–graphene oxide
Thermal conductivity (W mK^{-1})	0.373	0.488	0.506
Diffusion coefficient	0.076	0.012	0.008
Heat capacity in constant volume (kcal mol^{-1})	3.45×10^3	3.81×10^3	4.24×10^3

Fig. 17 (a) Paraffin-doped graphene nanocomposite structure (blue balls are hydrogen atoms, grey balls are carbon atoms, and red balls are dopant atoms); and (b) the temperature gradient result along the length of the nanocomposite. (c) Paraffin–graphene nanocomposite under tension (blue balls are hydrogen atoms and grey balls are carbon atoms). (d) Paraffin–graphene nano composites' stress–strain curves (this figure has been reproduced from ref. 76 with permission from Royal Society of Chemistry, copyright 2015).

alkane molecules), Tersoff (for BNNS and BNNT), and LJ (for interactions between n-eicosane molecules and boron nitride nanostructures). They constructed two types of n-eicosane system, amorphous structure and perfect crystalline structure (Fig. 18a and b). Fig. 18c and d show the structures of BNNS and BNNT respectively. Pure n-eicosane systems were minimized (energy minimization) using the conjugate-gradient algorithm.[129]

By adding BNNS and BNNT into n-eicosane paraffin, the thermal conductivity was fundamentally improved however latent heat was decreased. By increasing the temperature, the thermal conductivity of mixtures increased too, but for the perfect crystal decreased. The thermal conductivity of the amorph phase of the paraffin was independent of temperature change. This increase was greater before the melting point. Calculated thermal conductivities (in $T = 270$ K) were 0.33 W mK^{-1} for pure n-eicosane with a perfect crystalline structure,

0.14 W mK^{-1} for amorphous structure, 4.77 W mK^{-1} for the mixture of paraffin–BNNS, and 5.18 W mK^{-1} for the paraffin–BNNT mixture.

Li et al.[78] researched an n-octadecane–Cu nanocomposite system for studying its thermal properties. The diffusion coefficient at different temperatures showed that the n-octadecane–Cu nanofluid melting point increases with the increase of the Cu nanoparticle mass ratio. A similar trend for heat capacity and thermal conductivity was also found. Liu and Rao[79] investigated the interaction of n-octadecane with a surface of copper. Also, they studied the addition of a single-wall carbon nanotube in paraffin on the copper surface. They observed that paraffin molecules next to the copper surface were shaped in an orderly manner. So, the thermal conductivity increased. Also, after the addition of CNT, the orderly arrangement of paraffin molecules enhanced significantly and the phase transition temperature increased too. Yuan et al.[80] investigated n-octadecane paraffin
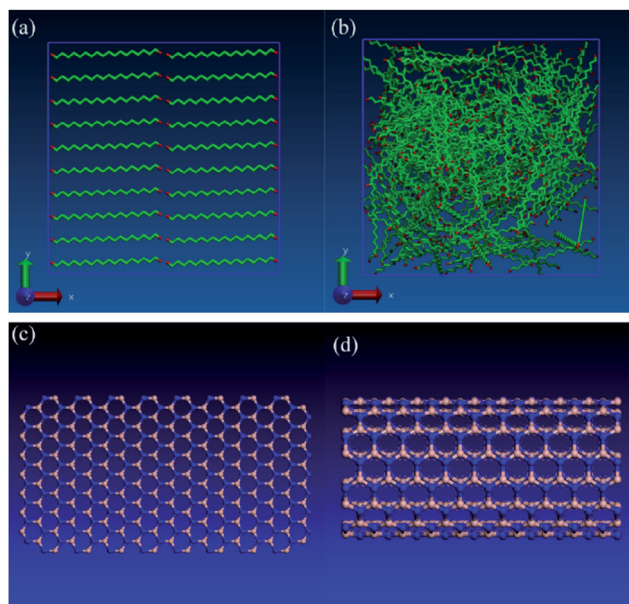
Fig. 18 (a) Perfect crystalline structure of pure *n*-eicosane system, (b) amorphous phase of pure *n*-eicosane, (c) boron nitride nanosheet (BNNS), (d) boron nitride nanotube (BNNT). The red atoms represent the methyl ($-CH_2-$) group and the green atoms represent the methylene ($-CH_3$) group. The color of nitrogen atoms is blue and the color of boron atoms is silver (this figure has been reproduced from ref. 77 with permission from Elsevier, copyright 2016).

containing pristine and functionalized graphene in different groups (hydroxyl, carboxyl, and ethyl groups). All constructed materials are shown in Fig. 19.

Simulations had done by Materials Studio software, using the COMPASS force field. The authors used non-equilibrium molecular dynamics (NEMD) simulation based on Muller–Plathe's method for thermal conductivity calculations. The thermal conductivity of the paraffin–pristine graphene system was 0.251 W mK^{-1} at 320 K. The thermal conductivity increased by functionalizing the graphene. With 10% functionalization coverage of graphene by hydroxyl, carboxyl and ethyl groups, the thermal conductivity of nanocomposites reached 0.33, 0.343, and 0.401 W mK^{-1} respectively. Moreover, with increasing coverage percent of graphene, the thermal conductivity was enhanced. The system functionalized by ethyl resulted in a 10 K increment in melting temperature, a 12% increment in the thermal capacity at 300 K, and a 59.8% increment in thermal conductivity at 320 K and these values were larger than that of the systems functionalized by ethyl and carboxyl. The molten salt phase change material, NaCl–SiO$_2$ composite, was simulated by Yu *et al.*[81] using a COMPASS force field. The configurations of simulation systems are shown in Fig. 20.

The outcomes demonstrated that NaCl thermal conductivity upgraded surprisingly. By adding a 2.4% volume fraction of SiO$_2$ nanoparticles, the thermal conductivity was enhanced 44.2%. The shear viscosity increased with the increment of the volume fraction of the nanoparticle, with a greatest mean increment of 23.6% with a 2.4% volume fraction of the SiO$_2$ nanoparticle. The melting point of NaCl–SiO$_2$ nanocomposite,

increased by increasing the SiO$_2$ volume fraction. Zhang *et al.*[82] conducted MD simulations to study the effect of graphene on *n*-pentacosane (C$_{25}$H$_{52}$) with ethylene-vinyl acetate (EVA) nanocomposites. The addition of 0.7 wt%, 1.5 wt%, 3.6 wt%, and 7.0 wt% of graphene to paraffin–EVA nanocomposite was simulated using Accelrys Materials Studio software. The UNIVERSAL force field (UFF) was utilized in the simulations.[74] Fig. 21a–c depict constructed materials for use in the simulations. The Muller–Plathe method was used for thermal conductivity calculations (Fig. 21d).

The calculated thermal conductivities of nanocomposite of 7% graphene and paraffin, were 0.4331 W mK^{-1}, 0.4117 W mK^{-1}, 0.4036 W mK^{-1}, 0.4503 W mK^{-1}, and 0.4086 W mK^{-1} at 313 K, 323 K, 333 K, 343 K, and 353 K, respectively. The addition of graphene to paraffin/EVA firstly enhanced the composite's thermal conductivity but then the thermal conductivity decreased in higher amounts of graphene. Authors declared that this is because of the presence of graphene on the vibration of molecules.

Paraffin (*n*-octadecane) containing CuO nanoparticles was studied by Zhao *et al.*[83] The CHARMM potential[58] was used in the LAMMPS package. First of all, the system was equilibrated at 373 K in a liquid state (Fig. 22a). Then to reach the solid state, the system was cooled down to 253 K (Fig. 22b).

The phase transition enthalpy change was calculated to obtain the enthalpy of melting. Fig. 22c shows the enthalpy of melting of different molar fractions of nanoparticles in nanocomposites.

The outcomes showed that the enthalpy of melting immediately diminished with the nanoparticle mass fraction increasing. For the nano-enhanced PCM with 19.72 wt% nanoparticles, the enthalpy of melting diminished by about 51.5%. When the system was in the liquid state, a dense phase was found around the nanoparticle. Molecules around the nanoparticles were in order and density. Authors expressed that the reason for NPCM melting enthalpy reduction is due to the reduction of paraffin molecules' number under the melting process.

Tafrishi *et al.*[84] investigated the influence of adding graphene and CNT to tetracosane paraffin (C$_{24}$H$_{50}$). The PCFF force field for paraffin, Tersoff potential (1989) for graphene and CNT,[127] and Lenard-Jones potential for van der Waals's interaction between nanoparticles and alkanoic material were used. PACKMOL package[130] was utilized to make the structures and the LAMMPS package for the simulations. Adding nanoparticles increased the density of the PCM. However, with enhancing the temperature, density decreased. The slope of density reduction for nanocomposites was less than that for pure paraffin. This was a positive point for adding nanofillers to phase change materials. Increasing the temperature influenced the arrangement of pure paraffin and the paraffin molecules became more irregular and amorphous. While the nanocomposite structures remained crystalline and regular. Furthermore, the thermal conductivity increased with adding graphene and CNT. However, the thermal capacity decreased. CNT was more effective than graphene for enhancing the thermal conductivity of paraffin. Also, thermal conductivity in the longitudinal
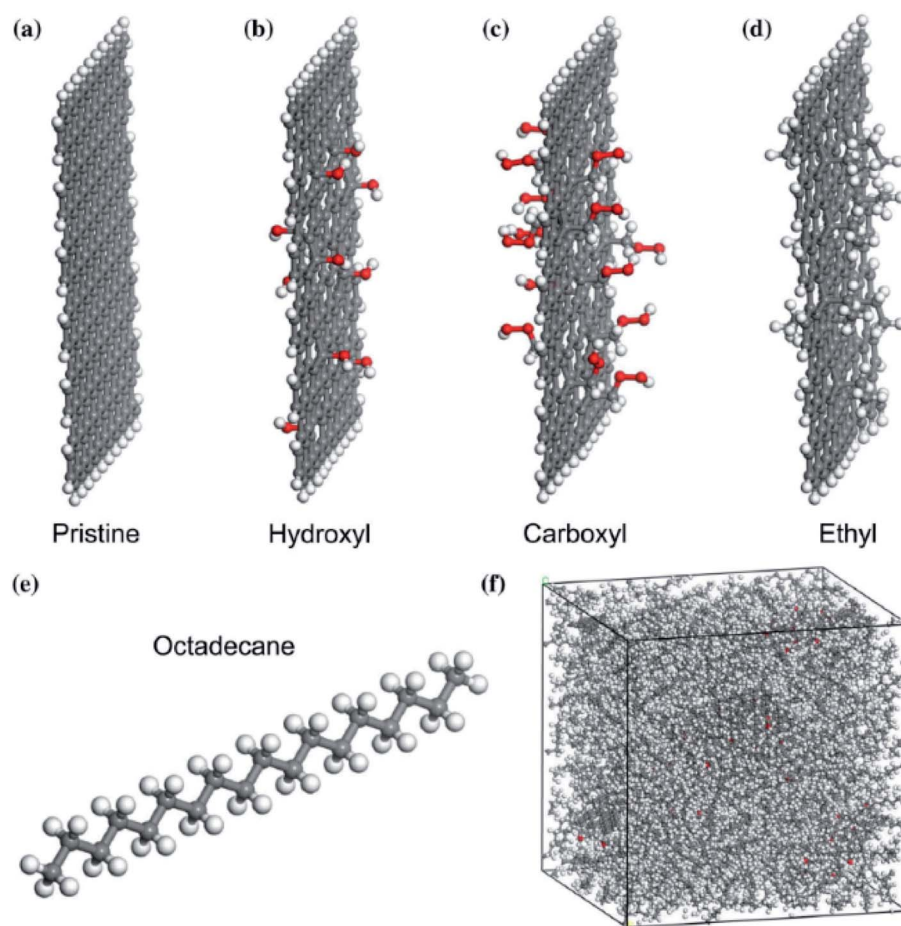
Fig. 19 The model of (a) pristine graphene and graphene functionalized with (b) hydroxyl, (c) carboxyl, (d) ethyl, (e) octadecane molecule, (f) configured composite system (gray balls are carbon atoms, white balls are hydrogen atoms, and red balls are oxygen atoms) (this figure has been reproduced from ref. 80 with permission from Springer Nature, copyright 2018).
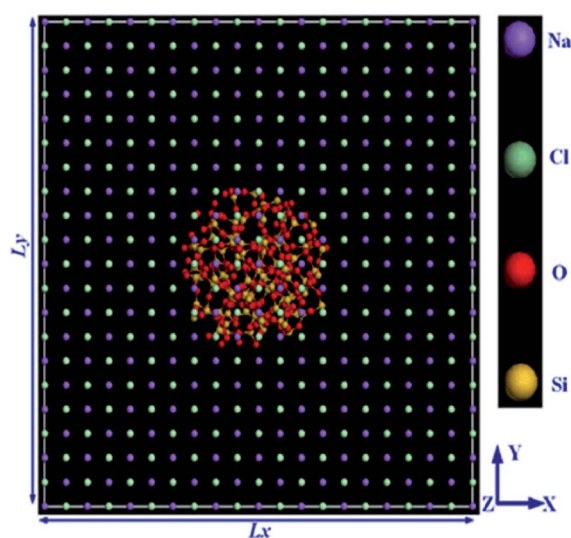

Fig. 20 The configuration of the simulation system (this figure has been reproduced from ref. 81 with permission from Elsevier, copyright 2019).

direction of graphene and CNT was more enhanced than in the perpendicular direction.

In another research, Tafrishi *et al.*[85] investigated the addition effects of hybrid nanoparticles to PCM. They added graphene and boron nitride nanosheets to octadecane paraffin. The utilized force fields were PCFF for paraffin, AIREBO for graphene, Tersoff for the boron nitride nanosheet, and Lennard-Jones for interactions between the nanoparticles and paraffin molecules. The structures of pure paraffin and nanocomposite PCM are shown in Fig. 23a and b, respectively.

The addition of nanofillers increased the density of PCM. Furthermore, enhancing the temperature decreased the density. This density change (reduction) for nanocomposite was less than that for pure PCM. MSD (mean square displacement) curves of pure and nanocomposite PCM showed that the nanocomposite's melting point was 10 K higher. The diffusion coefficient increased with temperature increasing, however, this value for nanocomposite was lower than that for pure PCM. So nanofillers reduce the atoms' movements and speeds. The thermal conductivity increased by the addition of nanofillers to paraffin by about 23.0 to 27.7% near the melting point. Besides, the thermal capacity of nanocomposite with hybrid nanoparticles
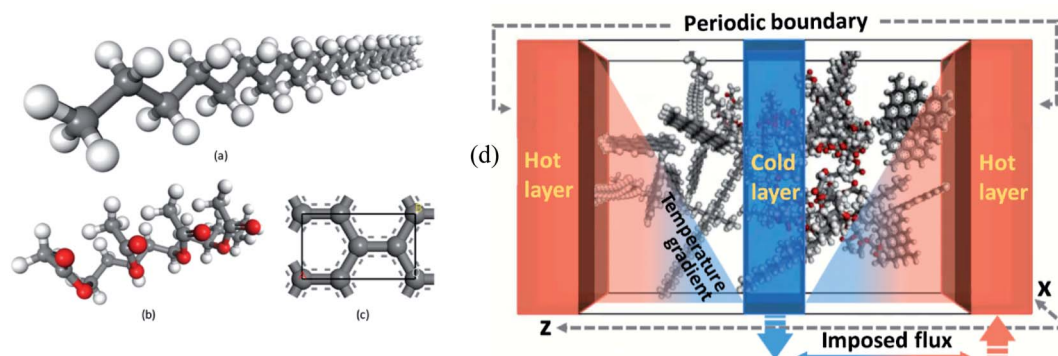
Fig. 21 The structures of (a) n-pentacosane paraffin, (b) ethylene-vinyl acetate (EVA) and (c) graphene lattice cell. (d) Schematic of thermal conductivity simulation using imposed flux method (this figure has been adapted from ref. 82 with permission from Elsevier, copyright 2019).
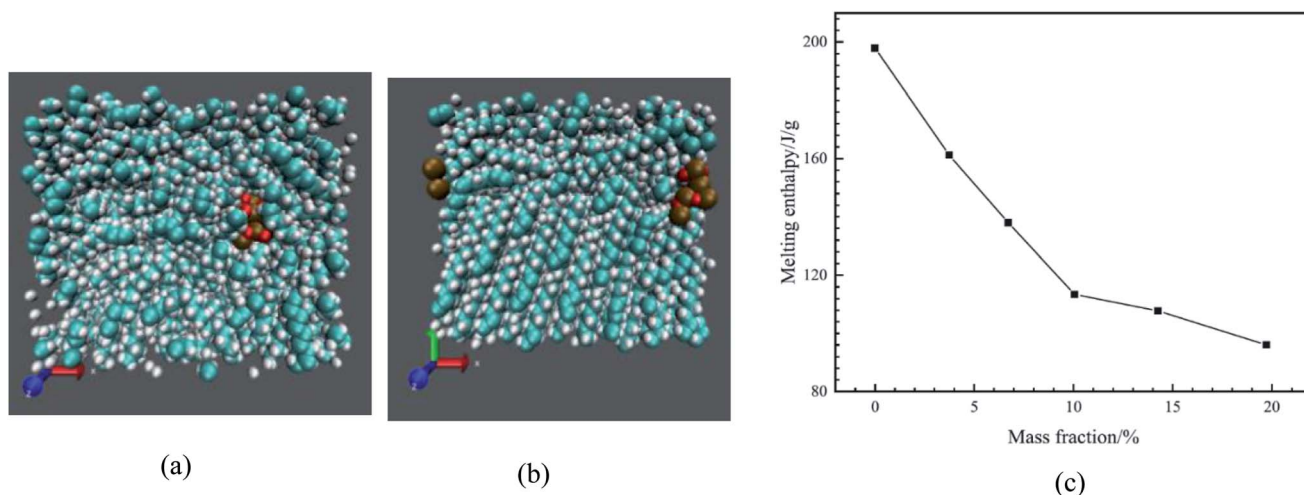

Fig. 22 Simulated nanocomposite system in solid (a) and liquid state (b) (cyan atoms are carbon, white atoms are hydrogen, ochre atoms are copper, and red atoms are oxygen). (c) Enthalpy of melting of nano-enhanced PCMs (this figure has been adapted from ref. 83 with permission from Elsevier, copyright 2020).
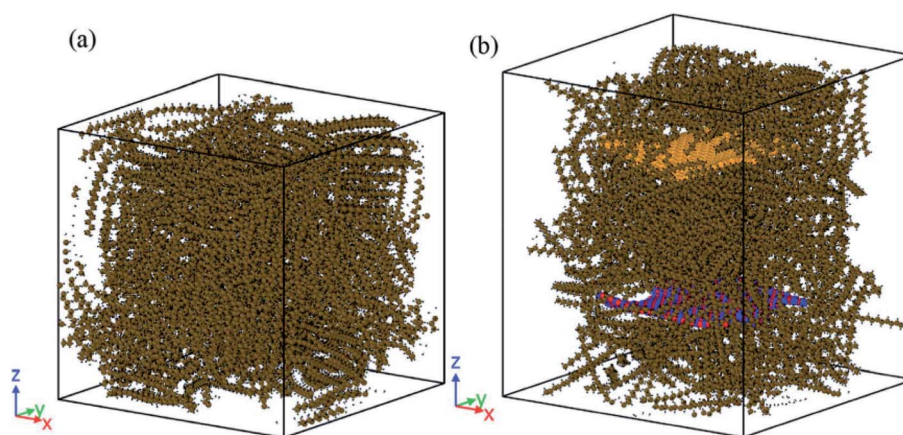

Fig. 23 Structures of: (a) the pure n-octadecane and (b) nanocomposite PCM utilized in the simulations (this figure has been reproduced from ref. 85 with permission from Royal Society of Chemistry, copyright 2020).

was higher than that for pure PCM. The addition of hybrid nanoparticles to phase change materials needs more research to obtain more results about the different thermal and mechanical properties of these nano-enhanced PCMs. Paraffin confined in slit-shaped pores of graphene sheets was investigated by Tong *et al.*[86] The melting point of n-eicosane paraffin was increased

due to the graphene interface. Paraffin molecules were arranged orderly in both solid and liquid phases. Molecules were almost parallel to graphene sheets. So, the melting was harder than solidification for this orderly arrangement of molecules.

Wang *et al.*[87] studied *n*-eicosane containing four different nanoparticles: nano-silver particles, nano-copper particles, nano-aluminum particles, and nano-iron particles. Self-diffusion coefficient increased by increasing the temperature. The radial distribution function showed that adding nano-particles increase the number of molecules around them. Also, the addition of nanoparticles resulted in a more compact system of PCM molecules. Interfacial thermal conductance between paraffin (*n*-octadecane) molecules and layers of boron nitride was calculated by Liu and Rao[89] with the nonequilibrium MD method. Size effect, BN layer number, arrangement of paraffin molecules, and the modified defects with various functional groups were investigated. Fig. 24 shows the simulated systems.

Rising the temperature enhanced the interfacial thermal conductance, however, the effect of size was inconspicuous. The largest interfacial thermal conductance occurred when paraffin molecules were parallel to the boron nitride surface. Furthermore, by increasing the number of boron nitride layers, the interfacial thermal conductance was reduced. Also, modified defects with functional groups (like hydrogen atoms) enhanced the interfacial thermal conductance. Zhao *et al.*[90] studied the effect of CuO addition to paraffin on its thermal behaviors. Fig. 25 shows a paraffin (*n*-octadecane) molecule and the simulated CuO nanoparticle.

The addition of CuO nanoparticles enhanced the thermal conductivity of PCM, and this addition was intensified with increasing the temperature and CuO mass fraction. This enhancement was weaker at lower temperatures and high CuO loadings. PDOS calculations showed that the thermal conductivity of nanocomposite PCM diminished along the direction departed from the CuO nanoparticle. Paraffin nanolayer was observed around the CuO nanoparticle and with increasing the size of CuO, the thickness of the nanolayer enhanced. The phonon scattering decreased due to the existence of a nanolayer around the CuO. This was the internal mechanism for the thermal conductivity of nanocomposite PCM.

Yu *et al.*[93] studied NaCl molten salt containing a CNT. The used potentials were Born–Mayer–Huggins (BMH) potential[91,92] for NaCl, Airebo for CNT, and LJ potential for the interactions between the salt and CNT. The melting temperature of NaCl–CNT nanocomposite decreased in comparison with pure NaCl.
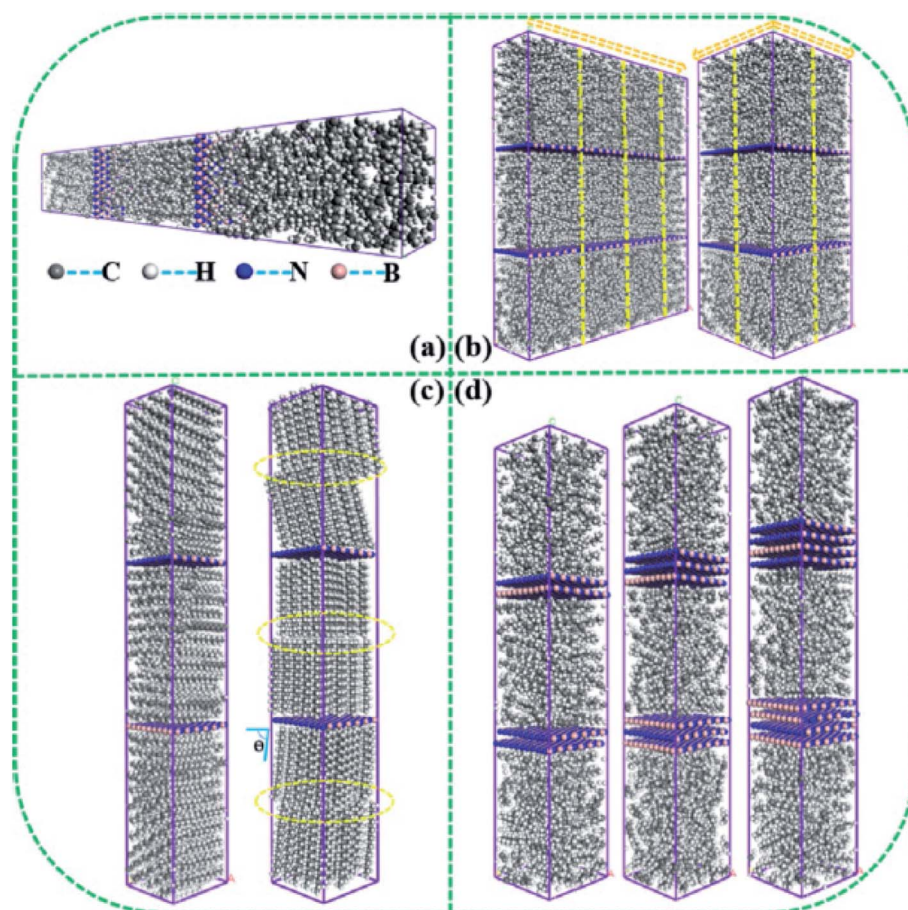

Fig. 24 Structures of *n*-octadecane paraffin with boron-nitride layers used in the simulations (this figure has been reproduced from ref. 89 with permission from Elsevier, copyright 2020).
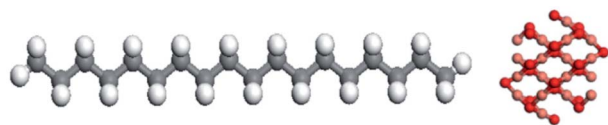
Fig. 25 Paraffin molecule structure (left) and CuO nanoparticle structure (right) (this figure has been reproduced from ref. 90 with permission from Elsevier, copyright 2021).

The addition of CNT reduced the self-diffusion coefficient of molten salt and with enhancing CNT mass fraction, this reduction intensified. The thermal conductivity of nano-composite was higher than that of pure molten salt. For example, 6.7 wt% CNT, increased the thermal conductivity by about 38.6%. But the melting enthalpy of nanocomposite was lower. For example, 6.7 wt% CNT, decreased the melting enthalpy by about 36.4%. Albeit the specific heat capacity was enhanced by about 5.9% by adding 6.7 wt% CNT. Jamshideasli et al.[94] investigated the interfacial thermal conductance of paraffin–graphene interfaces using NEMD simulations. Investigations were carried out by imposing a heat flux in both parallel and perpendicular configurations. Solid-phase nano-composite showed higher interfacial thermal conductance in comparison with liquid nanocomposite. By increasing the graphene layer numbers, the interfacial thermal conductance diminished.

Gu et al.[95] simulated capric acid–ethylene vinyl–graphene nanocomposite. By adding graphene up to 1.8 wt% the thermal conductivity increased, but after that, for higher graphene mass fractions decreased. MSD behavior was similar to that of thermal conductivity. Li et al.[96] studied the molecular dynamics simulation of n-eicosane paraffin containing functionalized graphene. Two kinds of oxygen functional groups were used on graphene surfaces with different ratios of epoxide and hydroxyl groups. With increasing the content of epoxide groups, the interfacial thermal resistance of nanocomposite PCM decreased firstly and then increased. Also, with increasing the epoxide groups content, the diffusion coefficient diminished. The melting point of nanocomposite containing functionalized graphene was lower than that for nanocomposite containing pristine graphene.

Wu et al.[97] studied the effect of size and layer number of boron nitride nanosheet (BNNS) on the thermal conductivity of paraffin. $C_{22}H_{46}$ paraffin was adopted as the matrix material. The studied sizes of boron nitride nanosheets were 9, 18, and 30 nm in length with 7 nm in width. By increasing the boron nitride layer number, the thermal conductivity increased and the interfacial thermal resistance between paraffin and the BNNS was reduced. By using 5 volume percent of BNNS, containing 15 layers, the thermal conductivity increased by 6 times compared to pure PCM. It reached 1.5 W mK^{-1}. The authors concluded that for enhancing the thermal conductivity of paraffin–BNNS nanocomposites, both the size and layer numbers of BNNS should be increased. n-Eicosane paraffin containing asphaltenes (natural aromatic polycyclic hydrocarbons) nanocomposites were studied by Glova et al.[101]

Asphaltenes could not improve the thermal conductivity of PCM. About this problem, the authors declared that the reason for this problem was due to the steric constraints imposed by the peripheral alkane groups, which prevented the formation of the extended ordered asphaltene aggregates. They proposed thermal cracking (dealkylation) of the asphaltene molecules by removing the lateral alkane groups from their aromatic cores. The modification method resulted in increasing the thermal conductivity by about 50–250%.

Tiantian et al.[102] simulated n-octadecane near graphite layers. Paraffin molecules arrangement was more regular near the graphene layers. By raising the temperature, the self-diffusion coefficient of paraffin molecules increased. Moreover, the self-diffusion coefficient of paraffin molecules staying far away from the graphite layers was higher than that of the molecules near the graphite layers. The thermal conductivity improvement was about 2.5 times higher because of the presence of graphite layers. Gao et al.[103] simulated palmitic acid (a fatty acid) containing graphene. The addition of 5 weight percent of graphene increased the thermal conductivity of
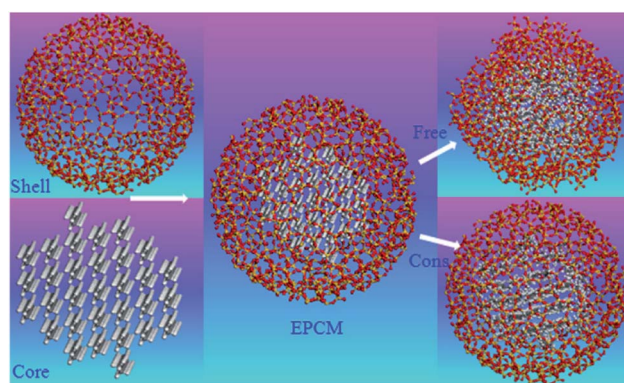

Fig. 26 The structures of nano-encapsulated phase change material (this figure has been reproduced from ref. 104 with permission from Elsevier, copyright 2012).
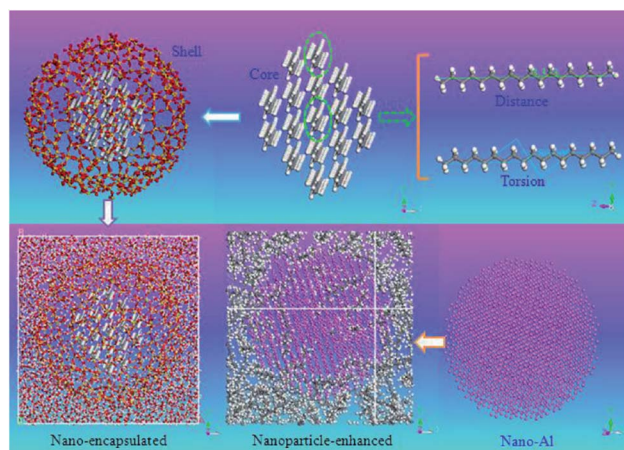

Fig. 27 Structures of constructed nano-encapsulated and nano-composite PCM (this figure has been reproduced from ref. 105 with permission from Elsevier, copyright 2013).

palmitic acid by about 36.4 and 40.4% in solid and liquid phases respectively. Moreover, the heat capacity of composite PCM increased in comparison with pure palmitic acid.

3.4 Nano/micro-encapsulated PCM simulations

Nano/micro-encapsulated PCM MD simulations will discuss in this section. Generally, traditional phase change materials, especially organic materials have some disadvantages such as low thermal conductivity, high change in density (and so volume) in melting range, flammability, sub-cooling, *etc.*[131] Macro, micro, and nano encapsulations of PCMs with polymer or inorganic shells are the technologies to overcome these problems.[132] Rao *et al.*[104] studied *n*-octadecane paraffin that was nano-encapsulated with a SiO$_2$ shell. They studied the melting behavior of PCM with constrained and free shells. The diameter

of the nano-capsule core was 4 nm while the shell's outer diameter was 5 nm. Fig. 26 shows the structures of simulated materials.

The used force field was COMPASS and the time step was 1 fs. The simulations were done using Materials Studio software. The constrained SiO$_2$ shell restricted the paraffin molecules, decreased their mobility and so resulted in a lower diffusion coefficient. However, the free and soft shell resulted in better thermal properties for energy storage. In another similar investigation, Rao *et al.*[105] studied the effect of shell thickness on the thermal properties of nano-encapsulated PCM. The capsule material was SiO$_2$ with a core of *n*-octadecane paraffin. Also, a nanocomposite PCM that was *n*-nonadecane paraffin containing Al nanoparticles was studied. Fig. 27 displays the constructed materials. The studied thicknesses of the shell of
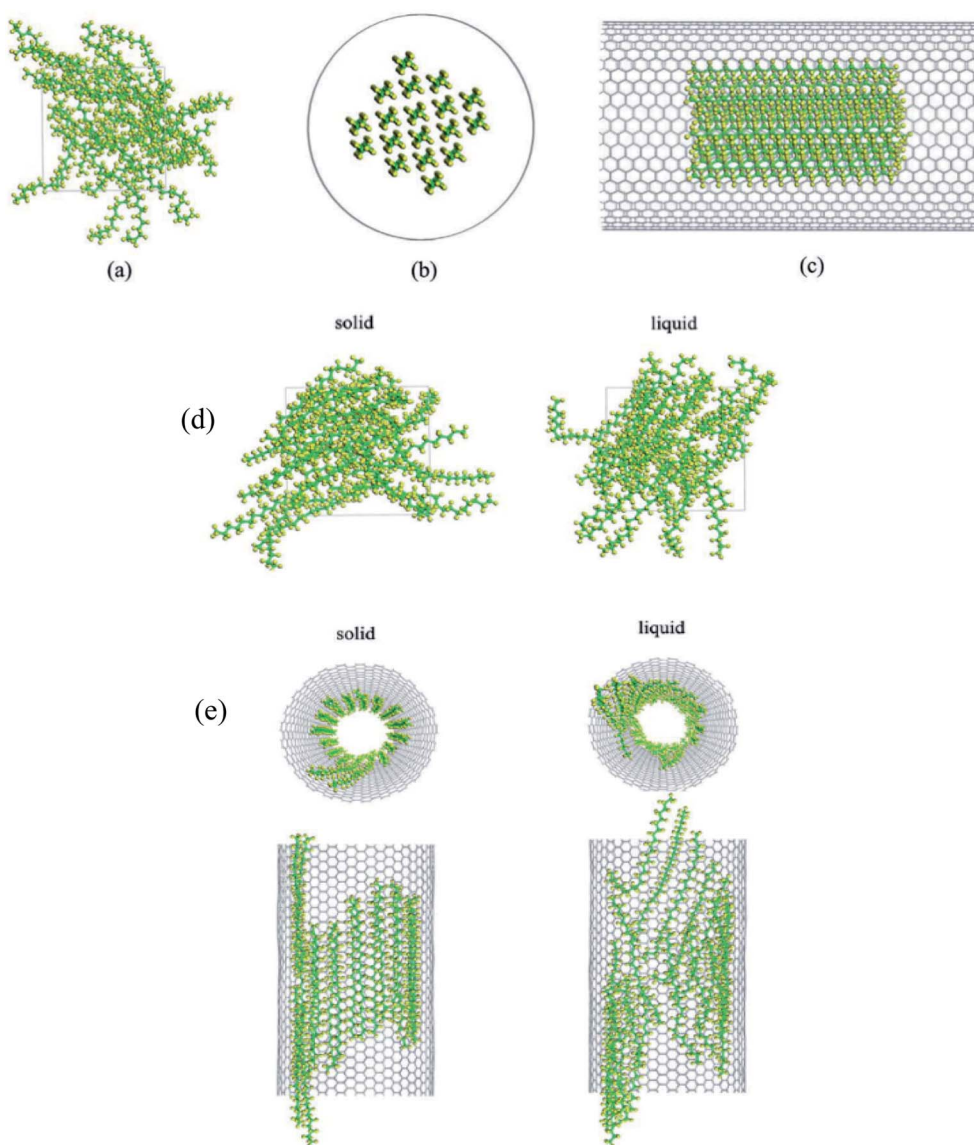

Fig. 28 The structures of (a) paraffin (*n*-hexacosane), (b) the cross-sectional view of paraffin encapsulated in a CNT, and (c) the side view of nano-encapsulated PCM. The structures of (d) pure paraffin and (e) nano-encapsulated paraffin with a CNT shell (this figure has been adapted from ref. 106 with permission from Royal Society of Chemistry, copyright 2015).
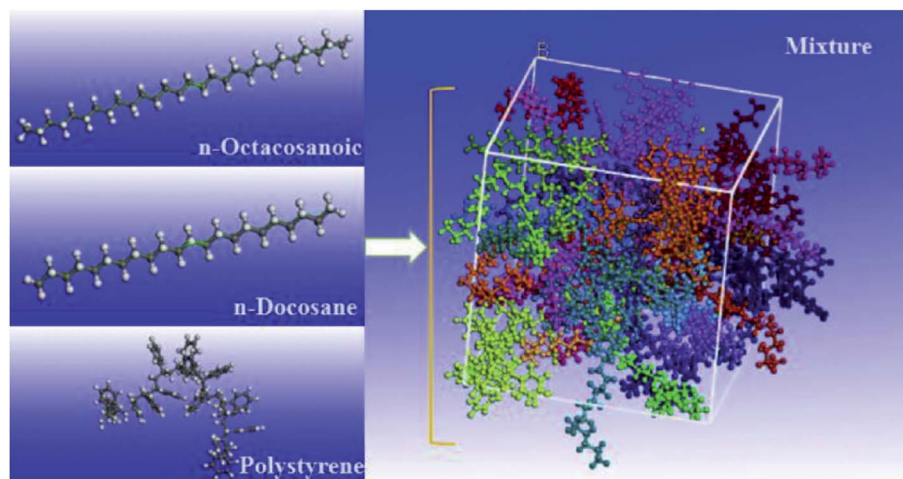
Fig. 29 The structures of *n*-octacosanoic, *n*-docosane, polystyrene, and their mixture (this figure has been reproduced from ref. 107 with permission from Elsevier, copyright 2017).

capsules were 0.8 nm, 0.6 nm, and 0.4 nm with a core of 4.2 nm. After the nano-encapsulation process, the nanocapsules were dispersed into water. Also, they studied the Al nanoparticle diameter effect that was 1 nm, 2 nm, 3 nm, and 4 nm.

Results showed that the change in shell thickness influences the radial distribution function and the diffusion coefficient. Reduced shell thickness caused a higher diffusion coefficient and higher stored thermal energy. However, the diffusion coefficient of the nanocomposite decreased by increasing the diameter of the Al nanoparticle. Nie *et al.*[106] studied *n*-hexacosane paraffin encapsulation inside a (25, 25) CNT. Fig. 28 displays the simulated structure.

Fig. 28d and e shows the simulated systems after running 1000 ps at 298 K and 358 K. Pure paraffin molecules were arranged in an irregular form, while the encapsulated ones were regular in an ordered manner. Besides, the arrangement of both systems in the solid phase was more regular than that of the liquid phase. Paraffin molecules in the CNT were spaced one by one and orientated regularly along the CNT inner wall. The degree of order diminished by raising the temperature. The self-diffusion coefficient of pure paraffin was lower than that for encapsulated paraffin. So the authors concluded that by encapsulating the paraffin, its molecular mobility and so the rate of heat transfer increases.[133]

The microencapsulated phase change materials (MEPCM) that constitute paraffin and polystyrene were considered by Liu *et al.*[107] *n*-Octacosanoic ($C_{28}H_{58}$), *n*-docosane ($C_{22}H_{46}$), and polystyrene were modeled for use in the simulations (Fig. 29).

Results showed that as temperature increased, the diffusion coefficient enhanced. In the melting range, the mobility and movement of molecules are enhanced intensely. However, the presence of polystyrene restricted the weak movement and vibration of PCM molecules. NEMD method was utilized for calculating the thermal conductivity of the system. The thermal conductivity of the composite PCM was lower than that of pure paraffin. Although, by increasing the temperature, the thermal conductivity was enhanced. One of the most common shell materials for use in nano and microcapsules is polyurethane.[134] Crosslinked polyurethane utilizes for its thermo-mechanical stabilized properties. Liu and Rao[108] constructed four kinds of
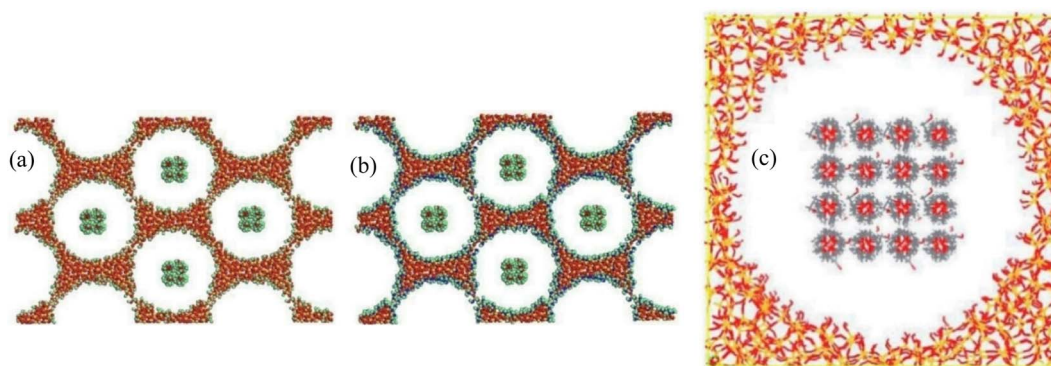

Fig. 30 Structures of porous (a) MCM-41-OH and (b) MCM-41-NH$_2$ (yellow atoms are silicon, red atoms are oxygen, blue atoms are nitrogen, and green atoms are hydrogen). (c) The unit cell of the PEG/MCM-41 structure (this figure has been adapted from ref. 110 with permission from Elsevier, copyright 2019).

polyurethane crosslinkers for molecular dynamics studying. The trihydroxy crosslinkers were based on diphenylmethane diisocyanate including glycerol, 1,2,6-hexanetriol, triethanolamine, and trimethylolpropane. The positions of hydroxyl groups, the type of crosslinkers, and the chain geometry had a direct impact on the structural properties. Hypercrosslinked polyurethanes had higher thermal conductivity and Young's and shear modulus compared to the low-crosslinked polyurethanes.

Abbaspour et al.[109] investigated the encapsulation of n-eicosane and n-octadecane paraffin in different CNTs. The effect of adding various metal nanoclusters (such as Cu, Ag, and Al) to encapsulated n-octadecane was studied. DL_POLY software was used for simulations.[135] The cutoff distance was 12 Å. The CNTs were kept fixed in the simulations. OPLSAA force field was utilized for simulating paraffin molecules. The Lennard-Jones potential with the Lorentz–Berthelot combination rules[136,137] was adopted to describe the interactions between paraffin and the CNT. Also, LJ potential was employed for the interactions between metal nanoclusters and paraffin. Strong metal interactions caused lower (more negative) energy in the systems which contained metal nanoclusters. Also, results indicated that a longer CNT has a lower melting point in comparison with the normal CNT system. Besides increasing the length and diameter of CNT enhanced the diffusion coefficient, while the addition of metal nanoparticles decreased the diffusion values. RDF curves exhibited significant changes in the melting point of paraffin–CNT in comparison with pure paraffin. Also, PCM nanocomposites containing metal nanoclusters had lower melting points in comparison with other systems. Al cluster system had the lowest melting point among all the simulated systems. Furthermore, melting caused decreasing in the order parameter of phase change nanocomposites.

3.5 PCM in porous media simulations

Nanoporous supporting materials have some benefits in the thermal energy storage field such as preventing liquid leakage, restricting the flow of liquid PCMs, and keeping PCMs in a macroscopic solid state during the phase change process. Also using nanoporous materials can significantly affect the PCM thermal properties such as solidification and melting enthalpy and melting and solidification point.[138,139] Therefore, understanding the molecular behaviors of PCM in the nanoporous supporting materials is necessary for creating high-performance nanoporous material-based PCMs. Nano/microporous media containing PCM will be discussed in this section. A new nanocomposite PCM was introduced by D. Feng et al.[110] PEG was the core and mesoporous silica MCM-41 was the matrix of this nanoporous media PCM. The inner channel surface of mesoporous silica was replaced with amino groups ($-NH_2$) instead of hydroxyl groups ($-OH$). Fig. 30a exhibits the mesoporous silica MCM-41 structure. The modified MCM-41-NH_2 is shown in Fig. 30b. The PEG/MCM-41 final structural composite model is displayed in Fig. 30c.

The employed force fields were CVFF, PCFF, and LJ for the interactions of MCM-41, PEG, and between MCM-41 and PEG,

respectively. Materials Studio and the LAMMPS package were employed for creating the models and molecular dynamics simulations, respectively. The time step was set as 0.1 fs. Researchers declared that for controlling the loading and crystallization behavior of PEG in MCM-41, the host–guest interactions could be adjusted by surface-modifying. Li et al.[111] studied the interactions between various C18 PCMs (stearic acid, octadecanol, octadecylamine, and octadecane) and methyl-modified CNTs. Fig. 31 displays the simulated structures of C18-PCM@CNT nanocomposites.

The interaction energy between the CNT and stearic acid molecules was the highest, followed by octadecanol molecules, octadecylamine molecules, and octadecane molecules. The gyration radius of molecules of stearic acid and CNTs was the highest, while octadecane molecules were the lowest. Stearic acid and octadecanol diffusion coefficients were small. This was because of the weak interaction between CNTs and octadecane molecules.

4 A molecular dynamics based grouping (PCM simulation table)

Table 7 provides a complete list of existing phase change materials with the melting point as well as the heat of fusion. With a not-so-catchy look, the human comfort temperature could be defined between 18 and 24 °C. The background color of this table is related to the operating temperatures related to the melting point of these materials.

As can be seen, materials such as glycerin, $NaCl\cdot Na_2SO_4\cdot 10H_2O$, $Mn(NO_3)_2\cdot 6H_2O/MnCl_2\cdot 4H_2O(4\%)$, polyethylene glycol, and paraffin 17-carbons could be listed as materials that used in building energy management. The temperature of these materials is highlighted in yellow. Therefore, in terms of
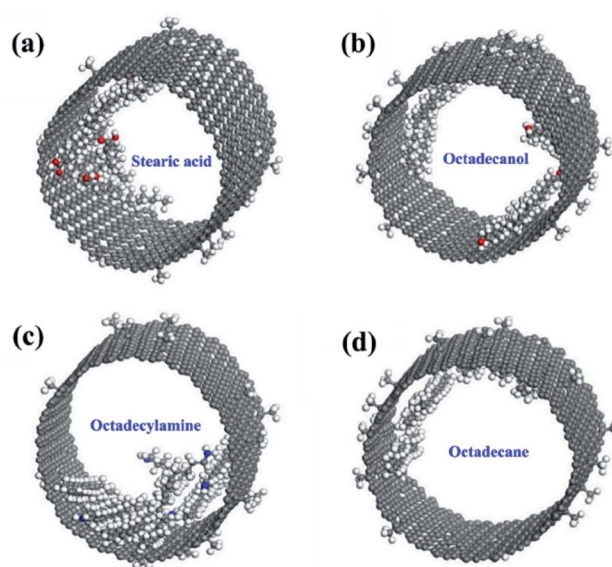

Fig. 31 The simulated structures of C18-PCMs@CNTs nanocomposite PCMs (this figure has been reproduced from ref. 111 with permission from Elsevier, copyright 2021).

Table 7 Structures, melting point, and heat of fusion of a complete list of existing phase change materials

application, these materials will have more applications in the future. Of course, materials with much lower or higher temperatures are also used for the human environment. But these materials are more important. These materials have simple structures and can be simulated using the hybrid potentials of PCFF and Leonard-Jones using the molecular dynamics method as one of the best force fields. Albeit, as listed in Table 1, several force fields were utilized for PCMs such as Snyder force field,[28] Ryckaert and Bellemans,[29,31] COMPASS,[41,45,51,65–67,70,78–81,87,96,102–108] PYS,[43,50] Weber,[47] Buckingham,[49,54] NERD,[53,68,71–73,86,94,97] EIM,[55] GROMOS,[57,60,61] CHARMM,[59,83,90] OPLSAA,[64,109] Universal force field (UFF),[75,82,95,111] PCFF,[37,76,84,85] TraPPE,[77] Dreiding,[89] Born–Mayer–Huggins (BMH),[93] GAFF,[98,101] CVFF.[110] Some of the utilized force fields were placed in the simulated material box of Table 8 in {} signs.

Therefore, they are mostly easy to study. These materials are suggested as the first suggestion for future works. In this table, structures with relatively longer chains are shown with a white background. These arrangements can also be simulated using the proposed potentials (PCFF + LJ). However, in terms of the number of particles involved in the simulation and the resulting high computational cost, they can create some challenges. Also, torsion and agglomeration of structures in these arrangements are very probable and precautions should be taken in this regard.

Since we need to take a closer look at the mentioned potentials (PCFF + LJ), here we simulate tetracosane paraffin, a relatively long-chain alkane with the chemical formula $C_{24}H_{50}$.

Table 8 Specifications of computer systems are used and related simulation times

System	RAM	CPU	Thermal conductivity (non-equilibrium)	Thermal conductivity (equilibrium)	Phase change simulation (melt and solidifying)
System 1: PC 1	8 GB	Intel-8 cores with 2.3 GHz	Pure: 80–123 Composite: 82	Pure: 85 Composite: 100	Pure: — Composite: 241
System 2: cluster	192 GB	Intel Haswell V3 28 core	Pure: — Composite: 13.5	Pure: — Composite: 7.5	Pure:— Composite: —

The molar mass of this alkane is 338.66 g mol^{-1}. As shown in Table 8, the melting point of tetracosane (PF 24 carbon) is about 50.6 °C. For a more detailed study, we have also studied the effect of adding nanomaterials to this phase change material to show that these systems can be studied with the same relatively available potential in any software. The type of nanoparticles studied in this research are graphene and carbon nanotubes.

VMD, msi2lmp, and packmol programs have been used to generate data files. The initial configuration of pure tetracosane containing 188 molecules of $C_{24}H_{50}$, containing 13 912 atoms, was made in a box with approximately $120 \times 10 \times 120$ (Å^3) according to Fig. 32. Then we made the data file of this structure (pure tetracosane) under the PCFF force field with the msi2lmp tool which contained 13 912 atoms, 13 724 atomic bonds (bands), 27 072 angles, and 38 916 dihedral and 18 048 improper. Data files of graphene-containing tetracosane nanocomposites, as well as carbon nanotubes, were made in the same way. Each of these composite structures also had 14 500 atoms. The percentage of nano-additives in the resulting composites was 10% by weight.

4.1 PCFF force field

The PCFF force field was used for interactions of alkane (paraffin tetracosane).[33–36] The Tersoff potential was used to describe the interaction of carbon atoms with each other in graphene and carbon nanotubes.[127] To calculate the forces between nanoparticles and alkane, the Lenard-Jones potential was used and its coefficients were extracted from the ref. 140. The Lorentz–Bertolet mix law[141] was used to determine the Leonard-Jones parameters between tetracosane and carbon atoms of nanomaterials. The PCFF force field is described in more detail here.

The functional form of the PCFF force field used is as follows (similar to the CFF force field):

$$E_{\text{total}} = \sum E^b + \sum E^a + \sum E^t + \sum E^o + \sum E^{bb'} + \sum E^{ba} + \sum E^{bt} + \sum E^{aa'} + \sum E^{at} + \sum E^{aa't} + \sum E^{\text{vdw}} + \sum E^{\text{elec}} \quad (7)$$

$$E^b = \sum_{n=2}^{4} k_n^b (b - b_0)^n$$
$$= \sum_b k_2 (b - b_0)^2 + k_3 (b - b_0)^3 + k_4 (b - b_0)^4 \quad (8)$$

$$E^a = \sum_{n=2}^{4} k_n^a (\theta - \theta_0)^n = \sum_\theta k_2 (\theta - \theta_0)^2 + k_3 (\theta - \theta_0)^3 + k_4 (\theta - \theta_0)^4 \quad (9)$$

$$E^t = \sum_{n=1}^{3} k_n^t (1 - \cos n\varnothing)$$
$$= \sum_\varnothing k_1 (1 - \cos \varnothing) + k_2 (1 - \cos 2\varnothing) + k_3 (1 - \cos 3\varnothing) \quad (10)$$

$$E^o = k^{(o)} (\chi - \chi_0)^2 = \sum_\chi k_2 \chi^2 \quad (11)$$

$$E^{bb'} = \sum_{n=1}^{3} k^{bb'} (b - b_0)\left(b' - b_0'\right) = \sum_{b,b'} k(b - b_0)\left(b' - b_0'\right) \quad (12)$$

$$E^{ba} = k^{ba}(b - b_0)(\theta - \theta_0) = \sum_{b,\theta} k(b - b_0)(\theta - \theta_0) \quad (13)$$

$$E^{aa'} = k^{aa'} (\theta - \theta_0)\left(\theta' - \theta_0'\right) = \sum_{\theta,\theta'} k(\theta - \theta_0)\left(\theta' - \theta_0'\right) \quad (14)$$

$$E^{bt} = (b - b_0) \sum_{n=1}^{3} k_n^{bt} \cos n\varnothing$$
$$= \sum_{b,\varnothing} (b - b_0)[k_1 \cos \varnothing + k_2 \cos 2\varnothing + k_3 \cos 3\varnothing] \quad (15)$$

$$E^{at} = (\theta - \theta_0) \sum_{n=1}^{3} k_n^{at} \cos n\varnothing$$
$$= \sum_{\theta,\varnothing} (\theta - \theta_0)[k_1 \cos \varnothing + k_2 \cos 2\varnothing + k_3 \cos 3\varnothing] \quad (16)$$

$$E^{aat} = k^{aat}(\theta - \theta_0)\left(\theta' - \theta_0'\right)\cos \varnothing = \sum_{\theta,\theta,\varnothing} k(\theta - \theta_0)\left(\theta' - \theta_0'\right)\cos \varnothing \quad (17)$$

$$E^{\text{vdw}} = \varepsilon \left[2\left(\frac{\sigma}{r_{ij}}\right)^9 - 3\left(\frac{\sigma}{r_{ij}}\right)^6 \right] \quad (18)$$
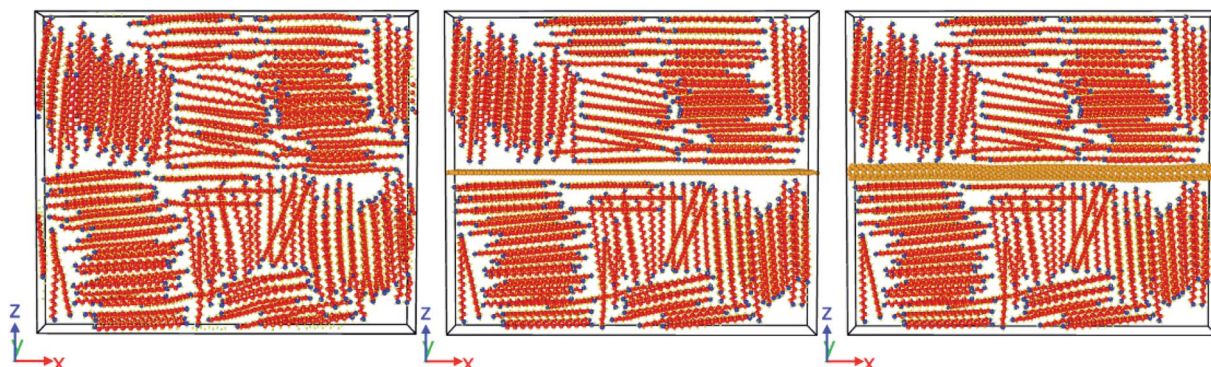

Fig. 32 Initial configuration of a box containing 188 molecules of tetracosane (left), tetracosane + graphene (middle), and tetracosane + carbon nanotubes (right).
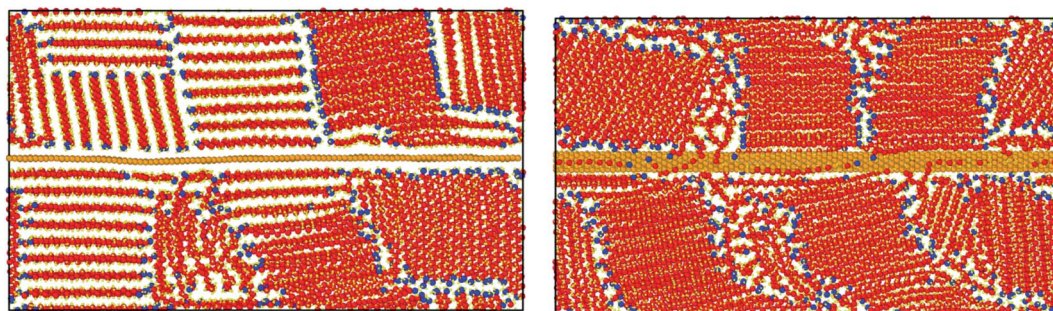
Fig. 33 Paraffin–graphene (left) and paraffin–carbon nanotube (right) composite structures after melting and freezing cycles.
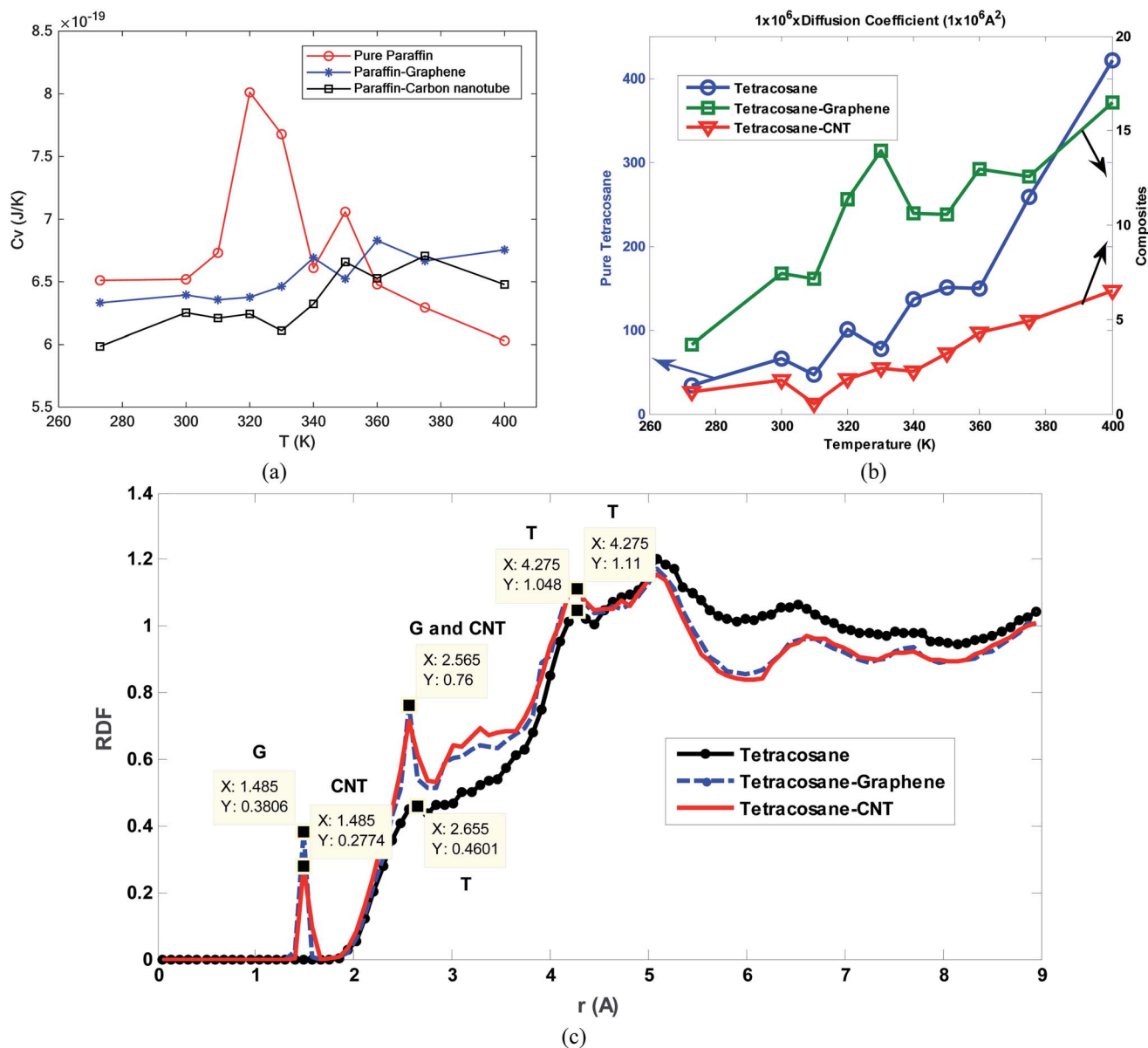

Fig. 34 The thermal capacity diagram in terms of temperature, diffusion coefficient, and radial distribution function for pure paraffin, paraffin–graphene, and paraffin–carbon nanotubes composites.

$$E^{\text{elec}} = \sum_{ij} \frac{q_i q_j}{r_{ij}} \qquad (19)$$

These functions can be divided into two main parts: valence and cross-coupling terms. Valence terms represent internal coordinates that include a bond (b), angle (θ), torsion angle ($\varnothing$), and off-plane angle (χ), and cross-coupling terms include combinations of two or three internal coordinates. Cross-coupling terms are important because they are used to predict system vibrational frequencies and structural changes. Fig. 33 shows paraffin–graphene and paraffin–carbon nanotube composite structures after melting and freezing cycles. Specifically, in both cases of adding graphene and nanotubes, the model was stable after the melting–freezing process.

4.2 Results obtained from the model used

As a small portion of the exciting results, the thermal capacity diagram in terms of temperature, diffusion coefficient, and radial distribution function for pure paraffin, paraffin–graphene, and paraffin–carbon nanotubes composites were plotted and compared in Fig. 34.

To evaluate the computational cost of the potential introduced, the specifications of the systems are used and the time spent are listed in Table 8. As distinguished, according to the ability of the systems used, the time spent on simulating the problem is low, and this is an acceptable cost range PCFF potential.

5 Research gaps

The number of publications on molecular dynamics of phase change materials is shown in Fig. 35. Although the number of published research was increasing in recent years, the researches number in this area is still very low. Most of these researches were about molecular dynamics simulation of paraffin (Fig. 36). Molecular dynamics study of other phase change materials is still a research gap.

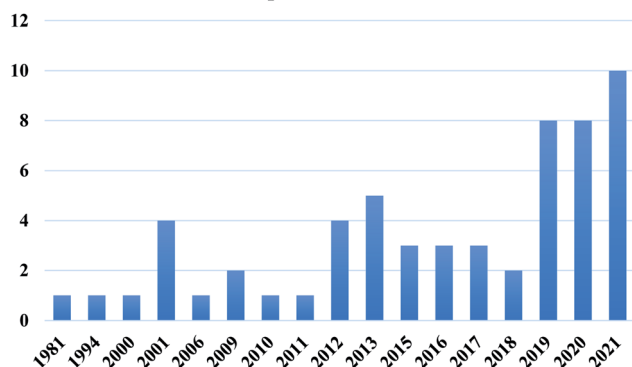**Fig. 35** Number of publications of molecular dynamics of phase change materials in recent years.
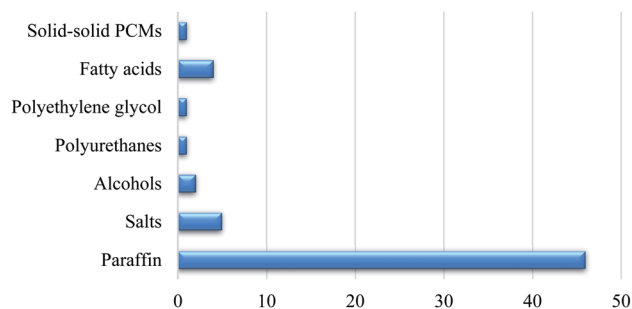

Fig. 36 Number of publications of molecular dynamics of different phase change materials.

Some other research gaps are as follows: addition of hybrid nanofillers to PCMs, porous media, new superconductive materials, new force fields, mass fraction influence, the combination of different types of PCMs together, research on the water as a good PCM with high latent heat, the influence of spacing of nanofillers in PCMs (like their shapes or their distance from each other), nano-encapsulated PCMs, nano-porous fillers and matrices, the effect of other atoms doped or adhesive to nanofillers, effects of the geometry of nanofillers and nanoporous matrices, effects of the distance of nanofillers (such as multilayer graphene with or without distance between layers or multiwalled CNTs, *etc.*), designing new nano-additives and new porous media or using new ones for PCMs or mixture of PCMs to acquire better thermo-physical properties, *etc.*

6 Conclusion

Phase change materials are used for thermal energy storage. Molecular dynamics simulations can reveal the thermal transport mechanisms of PCMs and this can be useful for producing better PCMs. In this paper, molecular dynamics studies of PCMs are described and thermal transport mechanisms are focused to understand the behaviors of the materials on the nanoscale. MD simulations of pure PCMs, mixed PCMs, PCMs containing nanofillers, nano-encapsulated PCMs, and PCMs in nano/microporous materials were investigated and the results are discussed. The thermal conductivity of nano-enhanced PCMs was one of the most important studied features. This can be increased on a nano-scale by the orientation of molecules (in molecular PCM systems). Thermal capacity, especially in the phase change temperature range, is another important characteristic that should be investigated in more investigations. Some of the used methods for enhancing thermal conductivity resulted in reduced thermal capacity. More investigations are required for better understanding and designing new nano-enhanced phase change materials with better thermal energy storage characteristics. A molecular dynamics-based grouping (PCM simulation table) was presented that is very useful for the future roadmap of PCM's simulation. In the

end, the PCFF force field was presented in detail and a case problem was studied for more clarity.

Data availability

The data that support the findings of this study are available on request from the corresponding author.

Conflicts of interest

There are no conflicts to declare.

References

1 K. Kalyanasundaram and M. Grätzel, *J. Mater. Chem.*, 2012, **22**, 24190–24194.

2 S. M. Hasnain, *Energy Convers. Manage.*, 1998, **39**, 1127–1138.

3 A. Sharma, V. V. Tyagi, C. R. Chen and D. Buddhi, *Renewable Sustainable Energy Rev.*, 2009, **13**, 318–345.

4 L. M. Bal, S. Satya and S. N. Naik, *Renewable Sustainable Energy Rev.*, 2010, **14**, 2298–2314.

5 K. Pielichowska and K. Pielichowski, *Prog. Mater. Sci.*, 2014, **65**, 67–123.

6 M. M. Farid, A. M. Khudhair, S. A. K. Razack and S. Al-Hallaj, *Energy Convers. Manage.*, 2004, **45**, 1597–1615.

7 H. Akeiber, P. Nejat, M. Z. A. Majid, M. A. Wahid, F. Jomehzadeh, I. Zeynali Famileh, J. K. Calautit, B. R. Hughes and S. A. Zaki, *Renewable Sustainable Energy Rev.*, 2016, **60**, 1470–1497.

8 B. Zalba, J. M. Marín, L. F. Cabeza and H. Mehling, *Appl. Therm. Eng.*, 2003, **23**, 251–283.

9 R. Parameshwaran and S. Kalaiselvam, in *Eco-Efficient Materials for Mitigating Building Cooling Needs*, ed. F. Pacheco-Torgal, J. A. Labrincha, L. F. Cabeza and C. G. Granqvist, Woodhead Publishing, Oxford, 2015, pp. 401–439, DOI: 10.1016/B978-1-78242-380-5.00015-7.

10 A. Kardam, S. S. Narayanan, N. Bhardwaj, D. Madhwal, P. Shukla, A. Verma and V. K. Jain, *RSC Adv.*, 2015, **5**, 56541–56548.

11 X. Fang, L.-W. Fan, Q. Ding, X. Wang, X.-L. Yao, J.-F. Hou, Z.-T. Yu, G.-H. Cheng, Y.-C. Hu and K.-F. Cen, *Energy Fuels*, 2013, **27**, 4041–4047.

12 S. Harish, D. Orejon, Y. Takata and M. Kohno, *Appl. Therm. Eng.*, 2015, **80**, 205–211.

13 M. Mehrali, S. Tahan Latibari, M. Mehrali, T. M. I. Mahlia, E. Sadeghinezhad and H. S. C. Metselaar, *Appl. Energy*, 2014, **135**, 339–349.

14 H. Ji, D. P. Sellan, M. T. Pettes, X. Kong, J. Ji, L. Shi and R. S. Ruoff, *Energy Environ. Sci.*, 2014, **7**, 1185–1192.

15 G.-Q. Qi, C.-L. Liang, R.-Y. Bao, Z.-Y. Liu, W. Yang, B.-H. Xie and M.-B. Yang, *Sol. Energy Mater. Sol. Cells*, 2014, **123**, 171–177.

16 S. Wu, H. Wang, S. Xiao and D. Zhu, *J. Therm. Anal. Calorim.*, 2011, **110**, 1127–1131.

17 R. Parameshwaran, K. Deepak, R. Saravanan and S. Kalaiselvam, *Appl. Energy*, 2014, **115**, 320–330.

18 R. Parameshwaran, P. Dhamodharan and S. Kalaiselvam, *Thermochim. Acta*, 2013, **573**, 106–120.

19 N. Metropolis, A. W. Rosenbluth, M. N. Rosenbluth, A. H. Teller and E. Teller, *J. Chem. Phys.*, 1953, **21**, 1087–1092.

20 B. J. Alder and T. E. Wainwright, *J. Chem. Phys.*, 1957, **27**, 1208–1209.

21 M. Micciarelli, B. F. E. Curchod, S. Bonella, C. Altucci, M. Valadan, U. Rothlisberger and I. Tavernelli, *J. Phys. Chem. A*, 2017, **121**, 3909–3917.

22 M. Valadan, E. Pomarico, B. Della Ventura, F. Gesuele, R. Velotta, A. Amoresano, G. Pinto, M. Chergui, R. Improta and C. Altucci, *Phys. Chem. Chem. Phys.*, 2019, **21**, 26301–26310.

23 M. Micciarelli, M. Valadan, B. Della Ventura, G. Di Fabio, L. De Napoli, S. Bonella, U. Röthlisberger, I. Tavernelli, C. Altucci and R. Velotta, *J. Phys. Chem. B*, 2014, **118**, 4983–4992.

24 M. A. González, *JDN*, 2011, **12**, 169–200.

25 P. K. Schelling, S. R. Phillpot and P. Keblinski, *Phys. Rev. B: Condens. Matter Mater. Phys.*, 2002, **65**, 144306.

26 D. P. Sellan, E. S. Landry, J. E. Turney, A. J. H. McGaughey and C. H. Amon, *Phys. Rev. B: Condens. Matter Mater. Phys.*, 2010, **81**, 214305.

27 R. G. Snyder, *J. Chem. Phys.*, 1967, **47**, 1316–1360.

28 G. Zerbi, R. Magni, M. Gussoni, K. H. Moritz, A. Bigotto and S. Dirlikov, *J. Chem. Phys.*, 1981, **75**, 3175–3194.

29 J. P. Ryckaert and A. Bellemans, *Chem. Phys. Lett.*, 1975, **30**, 123–125.

30 L. S. Tee, S. Gotoh and W. E. Stewart, *Ind. Eng. Chem. Fundam.*, 1966, **5**, 356–363.

31 K. Esselink, P. A. J. Hilbers and B. W. H. v. Beest, *J. Chem. Phys.*, 1994, **101**, 9033–9041.

32 T. Shimizu and T. Yamamoto, *J. Chem. Phys.*, 2000, **113**, 3351–3359.

33 H. Sun, *J. Phys. Chem. B*, 1998, **102**, 7338–7364.

34 H. Sun, *Macromolecules*, 1995, **28**, 701–712.

35 H. Sun, S. J. Mumby, J. R. Maple and A. T. Hagler, *J. Am. Chem. Soc.*, 1994, **116**, 2978–2987.

36 H. Sun, P. Ren and J. R. Fried, *Comput. Theor. Polym. Sci.*, 1998, **8**, 229–246.

37 Y. Tsuchiya, H. Hasegawa and T. Iwatsubo, *J. Chem. Phys.*, 2001, **114**, 2484–2488.

38 D. Rigby and R. J. Roe, *J. Chem. Phys.*, 1987, **87**, 7285–7292.

39 J. G. Harris, *J. Phys. Chem.*, 1992, **96**, 5077–5086.

40 H. Z. Li and T. Yamamoto, *J. Chem. Phys.*, 2001, **114**, 5774–5780.

41 I.-E. Mavrantza, D. Prentzas, V. G. Mavrantzas and C. Galiotis, *J. Chem. Phys.*, 2001, **115**, 3937–3950.

42 W. Paul, D. Y. Yoon and G. D. Smith, *J. Chem. Phys.*, 1995, **103**, 1702–1709.

43 N. Waheed, M. S. Lavine and G. C. Rutledge, *J. Chem. Phys.*, 2002, **116**, 2301–2309.

44 W. Smith and T. Forester, *DL_POLY_2.0: a general-purpose parallel molecular dynamics simulation package*, Warrington WA4 4AD, UK, 1996.

45 A. Marbeuf and R. Brown, *J. Chem. Phys.*, 2006, **124**, 054901.

46 T. A. Weber, *J. Chem. Phys.*, 1978, **69**, 2347–2354.

47 A. Diama, B. Matthies, K. W. Herwig, F. Y. Hansen, L. Criswell, H. Mo, M. Bai and H. Taub, *J. Chem. Phys.*, 2009, **131**, 084707.

48 S. Plimpton, *J. Comput. Phys.*, 1995, **117**, 1–19.

49 S. Jayaraman, A. P. Thompson, O. A. von Lilienfeld and E. J. Maginn, *Ind. Eng. Chem. Res.*, 2010, **49**, 559–571.

50 P. Yi and G. C. Rutledge, *J. Chem. Phys.*, 2011, **135**, 024903.

51 Z. Rao, S. Wang and Y. Zhang, *Phase Transitions*, 2012, **85**, 400–408.

52 S. K. Nath, F. A. Escobedo and J. J. de Pablo, *J. Chem. Phys.*, 1998, **108**, 9905–9911.

53 R. Rastgarkafshgarkolaei, Y. Zeng and J. M. Khodadadi, *J. Appl. Phys.*, 2016, **119**, 205107.

54 H. Ni, J. Wu, Z. Sun, G. Lu and J. Yu, *Renewable Energy*, 2019, **136**, 955–967.

55 X. Cui, J. Zhu, H. Xu, X. Cheng and W. Zhou, *Int. J. Mod. Phys. B*, 2019, **33**, 1950088.

56 C. Oostenbrink, A. Villa, A. E. Mark and W. F. Van Gunsteren, *J. Comput. Chem.*, 2004, **25**, 1656–1676.

57 B. Feng, J. Tu, J.-W. Sun, L.-W. Fan and Y. Zeng, *Int. J. Heat Mass Transfer*, 2019, **141**, 789–798.

58 A. D. MacKerell, D. Bashford, M. Bellott, R. L. Dunbrack, J. D. Evanseck, M. J. Field, S. Fischer, J. Gao, H. Guo, S. Ha, D. Joseph-McCarthy, L. Kuchnir, K. Kuczera, F. T. K. Lau, C. Mattos, S. Michnick, T. Ngo, D. T. Nguyen, B. Prodhom, W. E. Reiher, B. Roux, M. Schlenkrich, J. C. Smith, R. Stote, J. Straub, M. Watanabe, J. Wiórkiewicz-Kuczera, D. Yin and M. Karplus, *J. Phys. Chem. B*, 1998, **102**, 3586–3616.

59 Y. Feng, H. Zou, L. Qiu and X. Zhang, *Comput. Mater. Sci.*, 2019, **158**, 14–19.

60 B. Feng, L.-W. Fan and Y. Zeng, *Mater. Today Commun.*, 2020, **25**, 101335.

61 B. Feng, L.-W. Fan and Y. Zeng, *J. Heat Transfer*, 2020, **142**, 031401.

62 W. L. Jorgensen, D. S. Maxwell and J. Tirado-Rives, *J. Am. Chem. Soc.*, 1996, **118**, 11225–11236.

63 D. Tobias, K. Tu and M. Klein, *J. Chim. Phys.*, 1997, **94**, 1482–1502.

64 N. Wentzel and S. T. Milner, *J. Chem. Phys.*, 2010, **132**, 044901.

65 Z. Rao, S. Wang, M. Wu, Y. Zhang and F. Li, *Energy Convers. Manage.*, 2012, **64**, 152–156.

66 Z. Rao, S. Wang and F. Peng, *Int. J. Heat Mass Transfer*, 2013, **64**, 581–589.

67 Y. Wang, Z. Chen and X. Ling, *Appl. Therm. Eng.*, 2016, **98**, 835–840.

68 Y. Zeng and J. M. Khodadadi, *Energy Fuels*, 2018, **32**, 11253–11260.

69 S. J. Stuart, A. B. Tutein and J. A. Harrison, *J. Chem. Phys.*, 2000, **112**, 6472–6486.

70 T. Luo and J. R. Lloyd, *Adv. Funct. Mater.*, 2012, **22**, 2495–2502.

71 H. Babaei, P. Keblinski and J. M. Khodadadi, *Int. J. Heat Mass Transfer*, 2013, **58**, 209–216.

72 H. Babaei, P. Keblinski and J. M. Khodadadi, *Phys. Lett. A*, 2013, **377**, 1358–1361.

73 H. Babaei, P. Keblinski and J. Khodadadi, *J. Appl. Phys.*, 2013, **113**, 084302.

74 A. K. Rappe, C. J. Casewit, K. S. Colwell, W. A. Goddard and W. M. Skiff, *J. Am. Chem. Soc.*, 1992, **114**, 10024–10035.

75 Y.-R. Huang, P.-H. Chuang and C.-L. Chen, *Int. J. Heat Mass Transfer*, 2015, **91**, 45–51.

76 Y. Wang, C. Yang, Y. Cheng and Y. Zhang, *RSC Adv.*, 2015, **5**, 82638–82644.

77 C. Lin and Z. Rao, *Appl. Therm. Eng.*, 2017, **110**, 1411–1419.

78 Q. Li, Y. Yu, Y. Liu, C. Liu and L. Lin, *Materials*, 2017, **10**, 38.

79 X. Liu and Z. Rao, *J. Energy Inst.*, 2019, **92**(1), 161–176.

80 P. Yuan, P. Zhang, T. Liang, S. Zhai and D. Yang, *J. Mater. Sci.*, 2019, **54**, 1488–1501.

81 Y. Yu, Y. Tao and Y.-L. He, *Appl. Therm. Eng.*, 2020, **166**, 114628.

82 M. Zhang, C. Wang, A. Luo, Z. Liu and X. Zhang, *Appl. Therm. Eng.*, 2020, **166**, 114639.

83 C. Y. Zhao, Y. B. Tao and Y. S. Yu, *Int. J. Heat Mass Transfer*, 2020, **150**, 119382.

84 H. Tafrishi, S. Sadeghzadeh, R. Ahmadi, F. Molaei, F. Yousefi and H. Hassanloo, *J. Energy Storage*, 2020, **29**, 101321.

85 H. Tafrishi, S. Sadeghzadeh, F. Molaei and H. Siavoshi, *RSC Adv.*, 2020, **10**, 14785–14793.

86 X. Tong, P. Yang, M. Zeng and Q. Wang, *Langmuir*, 2020, **36**, 8422–8434.

87 X. Wang, L. Sun, X. Zhang, S. Zhang, J. Wang and Y. Zhang, *J. Mol. Liq.*, 2020, **309**, 113162.

88 S. L. Mayo, B. D. Olafson and W. A. Goddard, *J. Phys. Chem.*, 1990, **94**, 8897–8909.

89 X. Liu and Z. Rao, *J. Energy Storage*, 2020, **32**, 101860.

90 C. Y. Zhao, Y. B. Tao and Y. S. Yu, *J. Mol. Liq.*, 2021, **329**, 115448.

91 F. G. Fumi and M. P. Tosi, *J. Phys. Chem. Solids*, 1964, **25**, 31–43.

92 M. P. Tosi and F. G. Fumi, *J. Phys. Chem. Solids*, 1964, **25**, 45–52.

93 Y. Yu, C. Zhao, Y. Tao, X. Chen and Y.-L. He, *Appl. Energy*, 2021, **290**, 116799.

94 D. Jamshideasli, H. Babaei, P. Keblinski and J. M. Khodadadi, *J. Energy Storage*, 2021, **37**, 102469.

95 Y. Gu, L. Jiang, W. Jin, Z. Wei, X. Liu, M. Guo, K. Xia and L. Chen, *J. Ind. Eng. Chem.*, 2021, **99**, 256–263.

96 Y. Li, G. Yue, W. C. Tie, Q. Z. Zhu and T. Yan, *Int. J. Heat Mass Transfer*, 2021, **177**, 121533.

97 S. Wu, Q. Chen, D. Chen, D. Peng and Y. Ma, *J. Energy Storage*, 2021, **41**, 102931.

98 J. Wang, R. M. Wolf, J. W. Caldwell, P. A. Kollman and D. A. Case, *J. Comput. Chem.*, 2014, **25**, 1157–1174.

99 J. B. Klauda, R. M. Venable, J. A. Freites, J. W. O'Connor, D. J. Tobias, C. Mondragon-Ramirez, I. Vorobyov, A. D. MacKerell and R. W. Pastor, *J. Phys. Chem. B*, 2010, **114**, 7830–7843.

100 J. B. Klauda, B. R. Brooks, A. D. MacKerell, R. M. Venable and R. W. Pastor, *J. Phys. Chem. B*, 2005, **109**, 5300–5311.

101 A. D. Glova, V. M. Nazarychev, S. V. Larin, A. V. Lyulin, S. V. Lyulin and A. A. Gurtovenko, *J. Mol. Liq.*, 2021, 117112, DOI: **10.1016/j.molliq.2021.117112**.

102 T. Zhang, B. Xu and Z. Chen, *J. Therm. Sci.*, 2021, **30**, 1789–1802.

103 L. Gao, X. Fan, S. Zhang, D. Che and B. Sun, *Thermochim. Acta*, 2022, **707**, 179095.

104 Z. Rao, S. Wang and F. Peng, *Appl. Energy*, 2012, **100**, 303–308.

105 Z. Rao, S. Wang and F. Peng, *Int. J. Heat Mass Transfer*, 2013, **66**, 575–584.

106 C. Nie, X. Tong, S. Wu, S. Gong and D. Peng, *RSC Adv.*, 2015, **5**, 92812–92817.

107 X. Liu, C. Lin and Z. Rao, *J. Energy Inst.*, 2017, **90**, 534–543.

108 X. Liu and Z. Rao, *Int. J. Heat Mass Transfer*, 2019, **132**, 362–374.

109 M. Abbaspour, M. N. Jorabchi, H. Akbarzadeh and A. Ebrahimnejad, *RSC Adv.*, 2021, **11**, 24594–24606.

110 D. Feng, Y. Feng, P. Li, Y. Zang, C. Wang and X. Zhang, *Microporous Mesoporous Mater.*, 2020, **292**, 109756.

111 A. Li, G. Hai, P. Cheng, X. Chen, X. Zhang, Y. Jiang, Y. Gao, M. Huang and Y. Wan, *Ceram. Int.*, 2021, **47**, 23564–23570.

112 H. J. C. Berendsen, J. P. M. Postma, W. F. van Gunsteren, A. DiNola and J. R. Haak, *J. Chem. Phys.*, 1984, **81**, 3684–3690.

113 R. M. Lynden-Bell, J. S. Van Duijneveldt and D. Frenkel, *Mol. Phys.*, 1993, **80**, 801–814.

114 W. G. Hoover, *Phys. Rev. A: At., Mol., Opt. Phys.*, 1985, **31**, 1695–1697.

115 H. C. Andersen, *J. Chem. Phys.*, 1980, **72**, 2384–2393.

116 V. A. Harmandaris, V. G. Mavrantzas and D. N. Theodorou, *Macromolecules*, 1998, **31**, 7934–7943.

117 Accelrys Software Inc., *Discovery Studio Modeling Environment*, San Diego, CA, 2009.

118 L. Verlet, *Phys. Rev.*, 1967, **159**, 98–103.

119 M. Tuckerman, B. J. Berne and G. J. Martyna, *J. Chem. Phys.*, 1992, **97**, 1990–2001.

120 D. K. Benson, R. W. Burrows and J. D. Webb, *Sol. Energy Mater.*, 1986, **13**, 133–152.

121 J. Font, J. Muntasell, J. Navarro, J. L. Tamarit and J. Lloveras, *Sol. Energy Mater.*, 1987, **15**, 299–310.

122 G. Diarce, I. Gandarias, Á. Campos-Celador, A. García-Romero and U. J. Griesser, *Sol. Energy Mater. Sol. Cells*, 2015, **134**, 215–226.

123 C.-G. Tao, H.-J. Feng, J. Zhou, L.-H. Lv and X.-H. Lu, *Acta Phys.-Chim. Sin.*, 2009, **25**, 1373–1378.

124 C. F. Carlborg, J. Shiomi and S. Maruyama, *Phys. Rev. B: Condens. Matter Mater. Phys.*, 2008, **78**, 205406.

125 D. Rigby and R. J. Roe, *J. Chem. Phys.*, 1988, **89**, 5280–5290.

126 D. W. Brenner, O. A. Shenderova, J. A. Harrison, S. J. Stuart, B. Ni and S. B. Sinnott, *J. Phys.: Condens. Matter*, 2002, **14**, 783–802.

127 J. Tersoff, *Phys. Rev. B: Condens. Matter Mater. Phys.*, 1989, **39**, 5566–5568.

128 K. Matsunaga, C. Fisher and H. Matsubara, *Jpn. J. Appl. Phys.*, 2000, **39**, L48–L51.

129 M. C. Payne, M. P. Teter, D. C. Allan, T. A. Arias and J. D. Joannopoulos, *Rev. Mod. Phys.*, 1992, **64**, 1045–1097.

130 L. Martínez, R. Andrade, E. G. Birgin and J. M. Martínez, *J. Comput. Chem.*, 2009, **30**, 2157–2164.

131 C. Y. Zhao and G. H. Zhang, *Renewable Sustainable Energy Rev.*, 2011, **15**, 3813–3832.

132 V. V. Tyagi, S. C. Kaushik, S. K. Tyagi and T. Akiyama, *Renewable Sustainable Energy Rev.*, 2011, **15**, 1373–1391.

133 K. S. Hwang, S. P. Jang and S. U. S. Choi, *Int. J. Heat Mass Transfer*, 2009, **52**, 193–199.

134 A. Schoth, K. Landfester and R. Muñoz-Espí, *Langmuir*, 2015, **31**, 3784–3788.

135 I. T. Todorov, W. Smith, K. Trachenko and M. T. Dove, *J. Mater. Chem.*, 2006, **16**, 1911–1918.

136 M. Neek-Amal, R. Asgari and M. R. Rahimi Tabar, *Nanotechnology*, 2009, **20**, 135602.

137 K. Malek and M. Sahimi, *J. Chem. Phys.*, 2010, **132**, 014310.

138 H. Gao, J. Wang, X. Chen, G. Wang, X. Huang, A. Li and W. Dong, *Nano Energy*, 2018, **53**, 769–797.

139 D. Feng, Y. Feng, L. Qiu, P. Li, Y. Zang, H. Zou, Z. Yu and X. Zhang, *Renewable Sustainable Energy Rev.*, 2019, **109**, 578–605.

140 J. C. Grossman, N. Ferralis, D. Cohen-Tanugi and S. H. Dave, Materials and methods including nanoporous materials for water filtration, *US Pat.*, 15/634,767, 2014.

141 M. P. Allen and D. J. Tildesley, *Computer simulation of liquids*, Oxford University Press, 2017.